1993

Investigation into critical parameters which determine the oxygen refining capability of the slag during electroslag remelting of alloy 718

Dwight D. Wegman
Lehigh University

AUTHOR:

Wegman, Dwight D.

TITLE:

Investigation Into Critical Parameters Which Determine The Oxygen Refining Capability of The Slag During Electroslag Remelting of Alloy 718

DATE: May 30, 1993

INVESTIGATION INTO CRITICAL PARAMETERS WHICH DETERMINE THE OXYGEN REFINING CAPABILITY OF THE SLAG DURING ELECTROSLAG REMELTING OF ALLOY 718

by

Dwight D. Wegman

A Thesis

Presented to the Graduate and Research Committee

of Lehigh University

in Candidacy for the Degree of

Master of Science

in

Metallurgy and Materials Engineering

Lehigh University

1993

This thesis is accepted and approved in partial fulfillment of the requirements for the Master of Science.

May 7, 1993
Date

Thesis Advisor

Chairperson of Department

ACKNOWLEDGEMENTS

First and foremost, I wish to give thanks and honor to the Lord Jesus Christ for providing me with the ability and perseverance required to complete this thesis and program of study.

I also wish to thank Carpenter Technology Corporation for providing the opportunity and financial support in the completion of this program of study. In particular, I thank my superiors, Ron Gower, Sunil Widge, and Rich O'Hara for providing the motivational push and encouragement when I needed it. Gratitude is also extended to Mrs. Diane Dunkleberger for help in the preparation of the final document.

Appreciation is extended to my advisor, Prof. S. K. Tarby for his patience, encouragement, and helpful comments during the preparation of this thesis.

In conclusion, I also wish to thank my parents, Mr. and Mrs. Levi Wegman, for their faithful support and encouragement through the years and my wife, Sharon, whose encouragement and support were of immeasurable help during the completion of this thesis.

TABLE OF CONTENTS

LIST OF TABLES

LIST OF FIGURES

ABSTRACT

The ability to produce a very low oxygen activity in the slag during electroslag remelting of alloy 718 ingots was investigated. A low oxygen activity in the slag is desirable because it produces low oxygen levels in the remelted ingot and improves the cleanness of the material. Experimental parameters investigated during the study were: argon shrouding over the slag during remelting, aluminum and mischmetal deoxidant additions and, varied levels of CaO, La_2O_3 and Al_2O_3 in slag compositions. Data indicate that the use of oxides which are both basic and possess high negative free energies of formation will help to achieve the lowest possible slag oxygen activity and consequently, lowest ingot oxygen level. Ingot oxygen levels averaging only five ppm were obtained using these criteria in conjunction with argon shrouding.

In this study, measurement of the slag Fe_xO level was difficult and did not correlate well to ingot oxygen levels. Argon shrouding can improve control of slag/metal reactions and help to lower the slag oxygen activity, but can also be difficult to properly maintain during electroslag remelting.

Proper deoxidation of the slag also plays a significant role in achieving a low slag oxygen activity.

Gleeble hot ductility test data and actual heat forgability of alloy 718 ingots demonstrated mixed correlation. A large as-cast grain size was theorized to promote low melting point grain boundary eutectic phases of Ce and La which contributed to poor hot workability. Thus, the potential benefits of Ce and La to the refining capability of the slag can be compromised by their deleterious effect on hot ductility.

Oxides in the microstructure were generally on the order of a micron diameter and an insignificant microstructural feature. Volume percent oxide and oxide size demonstrated strong correlation while oxygen content and volume percent oxide also showed a weaker, but similar correlation. Future work to improve superalloy material cleanness should concentrate on the reduction of carbide/nitride clusters in the microstructure.

INTRODUCTION

Nickel base superalloys are an integral component of jet engine technology. As jet engine manufacturers seek to improve engine efficiencies, improve safety, and extend component life cycles, the level of cleanness in superalloys has become a major concern[1-3]. This concern stems from the fact that fatigue failures of superalloy jet engine components often originate with inclusions in the microstructure. These inclusions fall into two major categories - large oxides and clusters of titanium nitrides[1,2]. Minimizing the size and concentration of these inclusions in superalloys on a consistent basis through improved melting practices will achieve all three of the previously cited goals.

Wrought superalloys are generally manufactured using three different melting processes - Vacuum Induction Melting (VIM), ElectroSlag Remelting (ESR), and Vacuum Arc Remelting (VAR). Superalloys are melted using three different combinations of the above processes - VIM-VAR, VIM-ESR, and VIM-ESR-VAR. The VIM-VAR process has been the standard melting practice used for superalloys subjected to critical stress applications. Recently though, the triple melt process has become the preferred melting route in the

aerospace industry because of the extra ESR refining step which improves material cleanness.

The ESR process remelts an electrode by Joule or resistance heat which is generated when an electrical current, usually A. C., is passed through a fluoride/oxide slag to complete a circuit with the baseplate[4]. Since the molten slag has a higher melting point than the metal, molten metal droplets form at the bottom of the electrode that is immersed in the molten slag and drip through the slag to form a remelted ingot. Melting is performed within long cylindrical water cooled copper crucibles and movable mold furnaces which allow more flexibility to the process. ESR is a critical step within the superalloy melting process because it is usually the last step that can significantly refine the superalloy ingot by:

1. removing large oxide inclusions in the electrode from the primary VIM operation by dissolving them into the molten slag[5,6] and,
2. lowering the oxygen content of the superalloy.

VAR can remove a limited amount of oxygen and oxides, but does not have the potential to improve alloy cleanness to the extent that can be accomplished via ESR.

The use of an inert gas cover of argon over an ESR slag has been investigated at Carpenter Technology[7] and in the industry[8] as a means of improving control over the slag reactions which influence compositional control[4] and the refining capability of the slag. Previous work[7] at Carpenter showed that argon ESR had the potential of lowering the oxygen content of a nickel base 718 alloy 8" ingot to 5-10 ppm and improved the ingot cleanness compared to ESR under air. The current study further investigated the use of argon in combination with other slag modifications in an effort to improve the refining capability of the ESR slag and attain very low oxygen levels (<5 PPM) while maintaining compositional control during ESR.

Commercially, the ability to melt superclean superalloys via ESR is also attractive for two reasons:

1. The current designated superclean melting process of Electron Beam Cold Hearth Refining (EBCHR) is costly compared to the industry's current standard double and triple melting processes - VIM-VAR, VIM-ESR, VIM-ESR-VAR and,
2. EBCHR furnace capacity could not begin to meet the capacity demands of the superalloy industry.

The success of melting superclean superalloys via ESR would

allow the efficiency, safety, fatigue property, and economic benefits of superclean material to be realized using familiar industry technology and melting apparatus.

Specifically, the goals of this study sought to:

1. melt superclean Alloy 718 material having both an oxygen and sulfur content of <5 ppm.

2. better understand the role and interactions of the slag thermodynamic and thermochemical properties which determine the oxygen refining capability of the ESR slag.

3. maintain acceptable compositional control throughout the entire ingot.

PROCEDURE

A. Electroslag Remelting of Alloy 718

The experimental approach of this study focused on adjustments to the nominal $CaF_2/CaO/Al_2O_3$ slag composition and deoxidation practice used to electroslag remelt Alloy 718 with the intent of improving its refining ability. Improvements in this regard will improve the cleanness of the ingot. The literature[4,9-14] shows the crucial slag properties from a refining viewpoint are the slag basicity, FeO activity, and free energies of formation of the slag components. These slag properties determine the oxygen and sulfur contents of the molten metal as it is refined by the slag and thus dictate the oxide and sulfide inclusion content. In this study, the use of:

1. an argon cover to both eliminate atmospheric oxygen as a slag contaminant and gain control of slag reactions,

2. limited substitution of lanthanide oxides for Al_2O_3 in the slag composition,

3. slag deoxidation practices employing Al and mischmetal as deoxidants (Mischmetal is a master

alloy of rare earth elements containing approximately 50% Ce, 27% La, 16% Nd and other rare earth elements as the balance),

were all investigated as methods to lower the oxygen activity of the slag and consequently the oxygen content of the ingot. Ingots were melted sequentially based on information gained from prior heats.

All Alloy 718 material came from one VIM 10" electrode from heat 99776. Electrodes were 6" round diameter and were remelted into 7-5/8 or 8" round ingots in the R & D laboratory Consarc consumable electrode furnace. The furnace is an electrode withdrawal design and produces ingots of approximately 25" in length. Before ESR, the electrode chemical composition was analyzed at the top and bottom locations. Slag compositions were also analyzed before ESR. After ESR, chemical compositions were determined at A, B, C, and X ingot locations (see Figure 1). The composition of the slag cap was also analyzed after ESR. These data were necessary in order to determine what slag reactions were occurring during ESR.

The six 8" ingots of Alloy 718 remelted in this study were heats 1-6. The experimental parameters for the five

ESR heats and 1 VAR heat investigated and the corresponding goals for each heat were as follows:

Heat 1 - Nominal slag ($34CaF_2/27CaO/2.5MgO/30Al_2O_3/0.5SiO_2$) + 6% TiO_2 + 15 g Al/5 min melted under air cover.
Goal: To make an air-ESR ingot of balanced chemical composition for comparison purposes. This ingot represents a typical slag and deoxidation practice.

Heat 2 - Nominal slag + 4.5% TiO_2 + 4 g Al/5 min melted with argon shrouding.
Goal: To determine if the relatively low ingot oxygen results obtained in heat 1 could be improved upon with the use of an argon cover. Halfway through ESR of 2, a fuse failure in the furnace forced abortion of the heat. After repairs, the remainder of the electrode was remelted on top of the short ingot.

Heat 3 - Nominal slag + 4.5% TiO_2 + 25 g mischmetal/5 min melted with argon shrouding.
Goal - To determine if the oxygen activity of our nominal slag composition could be further lowered through use of a rare earth metal deoxidation addition.

Heat 4 - VAR.

Goal: To provide a VAR ingot of like size to the ESR ingots for comparison purposes.

Heat 5 - Lanthanide bearing slag ($31CaF_2/33CaO/8MgO/17.5La_2O_3/3.5TiO_2/0.5Al_2O_3/2SiO_2$) with argon shrouding - no deoxidation addition.

Goal: To determine if replacing the Al_2O_3 in the slag with La_2O_3 would lower the flux's oxygen activity and improve its refining capability.

Heat 6 - Rebalanced lanthanide bearing slag with small Al_2O_3 addition ($32CaF_2/38CaO/2MgO/16La_2O_3/2TiO_2/7.5Al_2O_3/0.5SiO_2$) with argon shrouding.

Goal: To determine if a very low oxygen ingot can be melted while maintaining compositional control of Al/Ti and minimizing La pickup in the ingot during ESR.

B. Ingot Sectioning and Microstructural Analysis

Following ESR, ingots were sectioned. As-cast discs were cold cut from the ingot at bottom, top and two interior locations as shown in Figure 1 utilizing a hem saw. These discs were used to obtain specimens for compositional, microstructural, and quantitative image analysis. After compositional analysis was completed, ingot sections of

comparable composition were selected from each of the five heats for Gleeble testing of hot ductility. Gleeble testing was chosen as a test method for this study because differences in inclusion content obtained from different ESR practices could influence the hot ductility of the respective ingots. It is possible that material containing a low inclusion level may demonstrate higher hot ductility compared to material containing a higher inclusion level.

Microstructural specimens were removed from the center of the A, B, C, and X discs of each ingot. These specimens were hot isostatically pressed at 2150F/1h/15ksi to eliminate all solidification porosity. Specimens were then automatically polished on the transverse orientation to a 0.05 micron finish and rated for oxide inclusion content via quantitative image analysis. Quantitative image analysis can determine the size and distribution characteristics of oxides by virtue of their contrast with the matrix. Past investigations have shown that reasonable correlations can be made between the oxygen level and oxide content of steels and superalloys[15-18]. Three different planes were polished and etched at each ingot location in an effort to generate more representative data. An average of 200 fields were examined at 2620X at each location to generate the statistical data reported for each location.

C. Gleeble Testing

All selected ingot sections were homogenized at 2175F/48h/Air Cooled (AC) to simulate the microstructural condition in which most superalloys are initially hot worked. Blanks of longitudinal orientation were cut from each section and machined into 0.252" rd. Gleeble test specimens to characterize the hot ductility of each of the respective heats. A machining diagram of a Gleeble hot ductility test specimen is shown in Figure 2. On-heating tests were conducted on one heat initially in order to determine the range of acceptable hot working temperatures for alloy 718. On-heating tests were performed at 1700, 1800, 1850, 1875, 1900, 2000, 2050, and 2100F for the initial heat. Single specimens were heated to the on-heating temperature, held for 5 minutes and pulled in tension at a strain rate of 1/second until fracture. The strain rate of 1/second was selected to simulate the strain rates typically observed during rotary forging of 718 alloy ingots. Hot ductility was measured by the percent reduction of area at the fracture location. From this series of on-heating tests, two on-heating temperatures were selected for the balance of the on-cooling Gleeble tests to be performed in the study.

Each ingot (ESR practice) was then tested in the following manner. Duplicate specimens from each ingot were tested at each of the two on-heating temperatures. On-cooling Gleeble tests were then conducted by heating the specimen to the predetermined on-heating temperature, stabilizing for 5 minutes at that temperature, cooling to the test temperature at 25 degrees F/second, stabilizing at the test temperature for 5 seconds and pulling the test specimen in tension at a strain rate of 1/second until fracture. On-cooling tests were conducted from 2000F down to 1600F in 100F increments. A few selected tests were also performed at 1950F. Hot ductility was determined by measuring the percent reduction of area at the fracture region in on-cooling specimens as well. Duplicate on-cooling Gleeble tests were performed where possible. However, testing was changed to single or sometimes triplicate samples depending on initial test scatter and availability of test specimens. Representative high, intermediate, and low ductility specimens were characterized via Scanning Electron Microscopy (SEM) analysis.

D. Pilot Bar Forging

Material from each of the five heats was also hot worked to evaluate the hot ductility. As-cast sections from each of the five heats were homogenized at 2175F/48h and air cooled. Sections of 3" x 3.5" x 5.5" were then cut from the as-cast plus homogenized ingots. Blocks were heated to 2050F, forged to an intermediate size of 1-1.5" sq. reheated to 1850F and finish forged to 0.75" sq.

RESULTS

Chemical compositions of each heat (before and after ESR) are listed in Tables I-VI. Slag compositions of the heats before and after ESR are provided in Tables VII-X, respectively. Details regarding voltage, current, power, and melt rate for the heats are provided in Table XI. A heat by heat summary containing details of the data are provided in the following text.

A. ESR - Heat 1

Data indicate that good control of Ti, Al, and Si levels was maintained during ESR. Ti, Al, and Si oxides all possess relatively high negative free energies of formation. Consequently, these three metallic elements are most prone to reactions with the $CaF_2/CaO/Al_2O_3$ slag and can be difficult to control during ESR if the slag composition is not in proper thermodynamic balance with the alloy. Sulfur contents ranged from 0.001 to 0.002% which is not as low as desired. Oxygen surprisingly, ranged from <5 to 13 ppm within the ingot which is lower than expected. It would appear that the slag deoxidation addition of 15 grams of Al/5 min deoxidized the slag well, but was not excessive since Al levels remained constant in the ingot. The

remaining elemental composition levels in the ingot basically remained unchanged after ESR. This heat does demonstrate that good compositional control of Ti, Al, and Si can be maintained during air ESR when a properly balanced slag composition and slag deoxidation practice are utilized.

The ESR voltage and current trace was rough with a wide "hash" in the beginning of the heat ("Hash" is a subjective description given to the range of current and voltage observed during ESR as recorded by the furnace controls on a strip chart). Once steady state conditions were attained though, the heat melted smoothly with a narrow hash for both voltage and current.

B. ESR - Heat 2

A lesser amount of Al was used in this heat to deoxidize the slag during ESR since an argon cover was being utilized. Ti and Al levels were properly balanced throughout melting indicating that the slag composition was in proper equilibrium. Sulfur levels were lowered below 5 ppm which is excellent. Oxygen levels ranged from 8 to 31 ppm and were higher than anticipated or desired. Other elemental levels remained unchanged. The high ingot oxygen levels indicate that the oxygen activity of the slag was higher than anticipated or desired. It is possible that

although an argon purge was utilized, it did not effectively isolate the slag from the atmosphere. Therefore, a higher Al deoxidation level would have deoxidized the slag more effectively and produced a lower oxygen level in the ingot.

Measurements of the exit gas from the furnace during ESR showed the oxygen content to be 1% or less for most of the melt. Fumes were also observed to evaporate from the slag and sometimes caused erratic exit gas oxygen readings. The argon flow rate was increased if exit gas oxygen readings became erratic. Ideally, it would be desirable to measure the oxygen content in the atmosphere at a position just above the slag. Unfortunately, practical limitations do not permit measurements of this type to be obtained and analysis of the exit gas purge is the best alternative. Originally, it was believed that since argon is heavier than air, it would automatically sink in the furnace and provide a good cover over the slag during ESR. These data suggest convective air currents above the slag may hinder effective argon shrouding and higher argon flow rates may be required to maintain an effective argon cover over the slag. If the slag did not have a good argon cover, this could explain why this ingot had higher than expected oxygen values.

After a rough start-up, this heat also melted smoothly with a narrow voltage and current "hash".

C. ESR - Heat 3

Data in Table III show that Si and Ti were in good control during ESR. Al fluctuated slightly more than desired, but also was still in reasonable control. If ingot Ti and Al levels are altered during ESR, usually Ti tends to increase while Al decreases. In this heat though, Al actually increased slightly during ESR. This trend reversal can be best explained as a result of the mischmetal deoxidation addition during ESR. Since CeO_2 and La_2O_3 possess higher negative free energies and consequently are more thermodynamically stable than Al_2O_3, the Ce and La deoxidant additions reduced some of the Al_2O_3 in the slag resulting in a slight pick-up in the ingot Al content. The deoxidation addition of 25 g/5 min may seem rather large compared to the amount used for Al. This was done because the respective atomic weights of Ce(140) and La(139) are almost 5.5 times higher than Al(26.9) and it was believed that this higher weight was needed to provide a similar level of deoxidation to the slag.

Sulfur levels were in the 4-5 ppm range which is excellent. However, oxygen values were disappointingly high at 40-56 ppm. Microstructural examination showed small inclusions dispersed both in the carbonitrides where they are normally found, but also in the matrix as well. SEM

analysis[19] of the inclusions showed them to be oxysulfides and phosphides which were enriched in Ce, La, Nd, and Ni. This observation indicates that the mischmetal addition utilized for heat 3 was excessive and produced rare earth oxysulfide and phosphide contamination in the microstructure of the ingot.

The exit gas oxygen analysis indicated that even though a higher argon flow rate was used than in past heats, it was more difficult to maintain oxygen levels below 2%. A second port closer to the crucible and slag cover was also utilized to measure oxygen content and showed higher than desired oxygen levels inside the crucible of 0.8% to 20% oxygen in spite of the increased argon purge rates. The excessive Ce and La mischmetal deoxidation additions and higher than desired oxygen levels above the slag probably combined to increase the ingot oxygen content to high levels.

As would be expected, there was also a slight pick-up of Ce (up to 390 ppm) and La (up to 200 ppm) in the ingot. A slight addition of lanthanides to superalloys is beneficial, but excessive amounts are deleterious to hot working and mechanical properties. At this point, it is not known above what level rare earth additions become deleterious to Alloy 718.

This heat demonstrated smooth melting behavior with a narrow voltage and current "hash" after start-up. The pick-up of CeO_2 to the slag did not produce any discernable effect on the voltage and current trace.

D. ESR - Heat 4

This heat was vacuum arc remelted for comparison purposes. It was decided that in order to perform an accurate evaluation of the ESR material, VAR material was needed. VAR proceeded smoothly with a narrow voltage and current trace and good vacuum integrity at all times. Compositional analysis data in Table IV show S levels to be 10-11 ppm which is slightly higher than observed in most ESR heats. Oxygen values fluctuated between <5 to 59 ppm. The high value of 59 ppm measured at the A location is probably not representative of the heat. Values of <5 to 22 ppm are believed to be more typical of VAR 718 material.

E. ESR - Heat 5

Data in Table V show that Ti and Al levels varied more than what was observed in the other Alloy 718 ESR heats. Ti levels were high and Al levels much lower than previously observed. These large compositional variations can be attributed to the experimental slag composition used for

this heat. The presence of approximately 16% La_2O_3 with no Al_2O_3 in the slag was responsible for the large Ti and Al fluctuations. Al from the ingot was oxidized into the slag which caused Ti and a small amount of La to be transferred to the ingot. It is well known that an ESR slag will react with the elements within the ingot composition until it has reached the "equilibrium" composition with respect to ingot material it is melting. As melting proceeds and the slag approaches its equilibrium concentration, less reaction occurs between the slag and ingot and less of the reactive element is transferred between the ingot or slag. This is why the Al depletion was much greater at the X location (0.25%) than at the A location (0.10%) of this heat. This was also confirmed by the slag analysis after ESR which showed the Al_2O_3 content increased by almost 7% (see Table IX). Si remained in good balance in the ingot.

The most encouraging data of this heat was in regard to the very low oxygen content obtained throughout the entire ingot. Data in Table V show that oxygen levels were in the vicinity of 5 ppm and less (the highest oxygen content observed was 6 ppm). These values meet the project goals and prove that it is possible to obtain very low oxygen levels in Alloy 718 via the ESR process. Sulfur levels were 6 ppm at all locations which is not quite as low as desired (<5 ppm), but are encouraging. Because Al from the ingot

was being absorbed into the slag to form Al_2O_3, a small amount of La was reduced and absorbed by the ingot. Table V shows that 100-180 ppm La was measured at each location. Again, it is not known if this level of La in Alloy 718 is deleterious to hot working and mechanical properties or not.

The exit gas oxygen level was measured to be approximately 8% at start, but steadily diminished till it was less than 2% by 25 minutes and remained there throughout the rest of the heat. This suggests that the actual slag composition may be a more important variable than the oxygen content above the slag. This is not to minimize the benefit of the argon cover to ESR, but to point out that a slag with a rare earth element component in it may be the more effective means of lowering oxygen content than by minimizing the oxygen content of the atmosphere above the slag.

This heat exhibited a rough current and voltage trace with wide hash from beginning to end. Current fluctuated as much as 1500 amps and voltage 8-9 V. As a result of this wide variation, the electrode feed into the slag was quite erratic as well.

F. ESR - Heat 6

The data in Table VI show that the Ti, Al, and Si levels in the ingot were all in good control. This result indicates that the lanthanide bearing slag with the 8% Al_2O_3 addition was close to the "equilibrium" slag composition required to melt Alloy 718 using a $CaF_2/La_2O_3/CaO$ bearing slag. Oxygen and sulfur levels were maintained at 7 ppm or less at all ingot locations and indicate that the oxygen and sulfur activities of the slag were kept to low levels during ESR.

The voltage and current trace from this heat was rough from beginning to end with wide hash similar to that observed in heat 5. Correspondingly, the electrode feed into the slag was also erratic. In addition, the ingot surface after ESR was also rather rough and irregular as compared to other heats melted in this study. The power data (kW) in Table XI show that this heat was melted with a lower power than heat 5 and suggests that the slag may have been too cold during ESR and produced this surface irregularity.

G. Microstructural Analysis

Microstructural specimens from each heat were examined to determine the effect of the various ESR refining processes on inclusion distribution within the microstructure. Figures 3-8 show representative unetched, 400X photomicrographs for heats 1-6. The five ESR heats (1-3,5,6) reveal varying amounts of oxides within the microstructure. Heat 5 contains the least oxides followed by heats 2,6, 1, and 3. Photomicrographs reveal that oxides are contained within nitrides and carbides and are not present in the general microstructure. The exception to this observation is heat 3 which was deoxidized during ESR with a mischmetal addition. The microstructure of heat 3 showed oxides were dispersed within the general microstructure and not confined within nitrides and carbides. Heat 4, representing the VIM-VAR practice generally shows a clean microstructure with few oxides.

The photomicrographs of Figures 3-8 are useful in exhibiting the general form of oxide precipitation in the microstructure, but do not provide a completely accurate indication of inclusion concentration because they only represent one field of view. The following section, which contains the quantitative image analysis data, does provide

a clearer indication of the true background inclusion level within the microstructure of each of the respective heats.

H. Quantitative Image Analysis Data

Oxide inclusion data were generated[20-24] and are listed in Tables XII-XVII, respectively. The volume percent oxide, number of particles/mm^2, average particle diameter (μm) and average particle area (μm^2) are provided for each heat. The corresponding oxygen value measured for each respective location is also included for comparison. The data show that the amount of oxide in all of the microstructures is quite low ranging from a minimum of 0.001% to a maximum of 0.023%. This result should be expected since all oxygen values were measured in the parts per million range. The average of each heat's data shows heat 5 to contain the least volume percent oxide, followed by heats 4, 2, 6, 1, and 3, respectively.

The average diameter and area of the oxides for heats 1-6 is in the vicinity of one micron and indicates that all oxides were rather small. The size of the oxides also generally agrees with the volume percent oxide measured, with heats containing the least volume percent oxide also exhibiting the smallest oxides. Re-examination of the ingot microstructures shown in Figures 3-8 indicates that the

oxides being measured are those contained within the carbides and nitrides. The one exception to this observation is heat 3 where more oxides are observed in the general microstructure than within nitrides and carbides.

I. Gleeble Test Data

Heat 4 (VIM-VAR) was selected for the initial series of on-heating Gleeble tests because it represents the standard melting process by which much premium alloy 718 is manufactured and, therefore, is an appropriate reference for the various ESR modifications. On-heating Gleeble test data for heat 4 are listed in Table XVIII and graphed in Figure 9. The data show that ductility is minimal at 2100F and 2050F, but begins to increase at temperatures under 2050F. Hot ductility appears to plateau at about 40% RA from 1900F to 1700F. Low ductility fractures at 2100F and 2050F demonstrated a dendritic surface morphology and sometimes fractured along a 45 degree shear angle. The 45 degree shear fracture exhibited smooth classic cleavage faces, whereas dendritic fractures exhibited more of an intergranular pattern which corresponded to primary and secondary dendrites. High ductility fractures showed a remnant dendritic structure, but with microvoid coalescence characteristic of higher ductility fractures. These low ductility data, particularly at 2050 and 2100F, were

surprising in that a 2050F hot working temperature is routinely utilized on large size 718 ingots and billets.

These data caused a dilemma in the selection of the two on-heating temperatures to be used for the balance of the on-cooling tests. Gleeble data from heat 4 indicated that 1950F and 1900F temperatures would be the proper on-heating temperatures. However, industrial practices routinely use forging temperatures of 2050F with good success and no forging problems. Press forging of an as-cast plus homogenized ingot section to 3/4" sq bar did not demonstrate any tearing as reported in the next section. Compositional checks were performed on forged bar and Gleeble specimen material from heats 3 and 4 to determine if a sample mix could have occurred during processing of the material. All forged bar and Gleeble composition data showed good agreement to the respective heat compositions and proved that sample mixing had not occurred. In order to make the information of this investigation of greatest utility to production manufacturing 718 practices, a decision was made to use 2000F and 2050F as on-heating temperatures for the balance of the on-cooling Gleeble tests of the study.

Gleeble ductility data for heats 1,3,4,5, and 6 are listed in Tables XIX-XXIII, respectively. Figures 10-14 also show graphs of the individual on-cooling ductility

behavior for each of the five heats. Figures 15 and 16 show on-cooling Gleeble ductility data graphed as a function of test temperature for two different preheating temperatures. As Tables XIX-XXIII show, both 2050 and 2000F preheating temperatures were utilized for Gleeble testing of specimens prior to cooling to the designated test temperature. Figure 15 shows the on-cooling ductility data of the five tested heats graphed as a function of the on-cooling test temperature for a 2050F preheat temperature. Figure 16 shows a similar graph for a 2000F preheat temperature. Generally, Figures 15 and 16 show that the highest hot ductility was experienced in heat 3, followed by heat 1, heat 6, heat 5, and heat 4 in descending order. It is also interesting to note in Figure 15 that the hot ductility of heat 3 drops off significantly at lower temperatures compared to the other heats. These differences in ductility indicate that the microstructure of the heats must have varied. Grain boundaries are the most likely location of this variation because the residual elements of interest in this study can influence the strength and integrity of the grain boundary and, consequently, the hot ductility.

Examination of the fracture face from a 0% Reduction of Area (RA) on-cooling Gleeble specimen (2050 --> 2000F) from heat 4 showed most of the fracture surface to be very smooth. A low magnification SEM photomicrograph is shown in

Figure 17[24]. Primary and secondary dendrites can be readily observed. This fracture morphology is characteristic of a cleavage fracture mechanism and confirms the 0% RA of the specimen. It would appear that the fracture progressed along the primary dendrites.

Figure 18 shows a heat 5 on-cooling Gleeble specimen (2050 -->1700F) which had 37.9% RA. Figure 18A shows the fracture occurred on a 45 degree angle suggesting that the fracture occurred on a shear plane. Figure 18B shows a slightly dimpled fracture surface which is characteristic of the higher ductility fracture mechanism of microvoid coalescence.

Figure 19 shows the fracture surface of a heat 5 on-cooling Gleeble specimen (2050 -->1700F) which had 53% RA. This is the same test condition as Figure 18, but demonstrated higher ductility. No evidence of a shear plane is observed and microvoids are present once again, but appear to be more elongated than the sister specimen. The more extensive and elongated dimpling contributed to this specimen's higher ductility.

Figure 20 shows the fracture surface of a heat 3 on-cooling Gleeble specimen (2050 -->1800F) which demonstrated a very high ductility of 87.9%. Extensive microvoid

coalescence can be observed over the entire fracture region. Thus, Gleeble specimen fracture faces reflected characteristic high and low ductility fracture face morphology.

J. Pilot Bar Forging

Forging results were as follows:

Heat 1 - no tearing observed during entire forging sequence,
Heat 3 - could not forge - tears developed immediately upon first reductions,
Heat 4 - no tearing observed during entire forging sequence,
Heat 5 - slight tearing during initial reduction, finish forged to 0.75" sq without further tearing,
Heat 6 - slight tearing on initial reduction, finish forged to 0.75" sq without further tearing.

Based upon the Gleeble on-cooling ductility data, the pilot bar forging results are rather surprising. Heat 3 which showed the best on-cooling ductility demonstrated very poor ductility and could not be hot worked. Also, heat 4 which demonstrated the poorest Gleeble hot ductility demonstrated good hot working behavior during forging. Heats 1,5, and 6 forging behavior demonstrated reasonable agreement with Gleeble on-cooling ductility values. A compositional check

was performed on Gleeble specimens from heats 3 and 4 to determine if oxygen, sulfur, Mg, Ca, Ce, and La values agreed with the respective heat compositions. Results showed that each Gleeble specimen composition agreed with the expected heat composition.

DISCUSSION OF RESULTS

The ability of a slag to remove oxygen from a metal/alloy during ESR is greatly influenced by the following slag properties:

1. basicity,
2. FeO activity (oxygen potential) and
3. free energy of formation of slag components.

Brief contemplation of the above criteria reveals that these slag properties are interdependent. Failure to meet the three criteria in the slag simultaneously during ESR will result in a slag with diminished refining capability. Thus, the data obtained by the various ESR melting procedures of this study reflect the ability (or inability) to meet the above criteria.

As each of these criteria is applied to the ESR heats melted in this study, understanding of the crucial factors affecting slag performance can be enhanced.

A. Effect of Slag FeO Content on Ingot Oxygen Content

It is well known that removal of oxygen during ESR is directly related to the FeO content of the slag. Figure 21[9] illustrates this effect quite well and shows that as the Fe_xO content decreases, the dissolved oxygen level within the metal pool also decreases. The reason why iron oxide plays such an important role in the ingot oxygen content can be attributed to the relative ease in which iron oxide can change valency state[4,12]. Hoyle[4] has outlined how iron oxide acts to transfer oxygen from the atmosphere above the slag to the ESR metal pool:

$Fe + 1/2O_2$ (g) --------> (FeO) electrode/slag/air interface

$2(FeO) + 1/2O_2$ (g) ------> (Fe_2O_3) slag/air interface

$(Fe_2O_3) + Fe$ ----------> 3(FeO) metal/slag interface.

Thus, it can be seen that iron oxide behaves as the medium through which oxygen is transferred from the atmosphere above the slag to the metal. Iron oxide also has a low solubility in CaF_2 which increases its activity and oxygen pick-up in the slag considerably[4,26]. Fortunately, CaO has been found to lower the activity of iron oxide and counteracts this deleterious effect.

Sasabe and Asamura[27] investigated oxygen transport from the atmosphere through a $CaO-SiO_2-Al_2O_3$ slag film and discovered that additions of CaF_2 and other oxides to metallurgical slags produced widely varying oxygen transport rates. Their work showed that iron oxide possessed the highest oxygen diffusion rate of all the oxides investigated as shown in Figure 22 and show that only a 0.2% Fe_2O_3 addition to the slag increased the reference oxygen diffusion rate dramatically.

Sasabe and Asamura[27] also discovered that transition metal oxides as a whole also possessed higher oxygen transport rates than non-transition metal oxides. For slags containing non-transition metal oxides such as Al_2O_3, their data showed that oxygen was absorbed into slags in the form of O_2 molecules with the diffusion rate directly proportional to the oxygen partial pressure. For slags containing transition metal oxides, oxygen was absorbed by the slag in the form of O^{-2} ions with corresponding positive holes. Diffusion rates into the slag followed a 1/n power dependence where n was the oxygen partial pressure above the slag. While the true magnitude of the oxygen diffusion rate increase due to the presence of Fe_2O_3 in the slag may be debated, the trend of higher oxygen transport rates with increasing levels of FeO in the slag appears genuine. Thus, slags containing high FeO levels will possess high oxygen

activities and produce higher than desired oxygen levels in remelted ingots. With respect to the current study, the implication is clear. Low oxygen partial pressures above the slag in combination with low slag FeO levels should produce ingots containing low oxygen levels.

With respect to the data of this study, slag analysis did not distinguish FeO from Fe_2O_3. Hence, it is difficult to develop a clear relationship between percent FeO and the oxygen content of the ingot. Figure 23 shows the total percent Fe_xO measured at the end of ESR with the oxygen content at the "A" location of the ingot. No discernable trend is evident. It is quite possible the percent Fe_xO contents measured in the slag are not a true indication of the percent FeO levels present during ESR. Unfortunately, the ESR furnace design does not permit slag samples to be taken in a practical manner during ESR and the slag analyses represent samples removed from the slag cap after ESR. It is also possible that the hot top procedure which gradually ramps down the power in order to terminate ESR could have altered the percent FeO content from the nominal percent FeO present during ESR. The data do show that heat 5 which had the lowest ingot oxygen level, also had the lowest measured Fe_xO level of all the slags at 0.03%. This result is contradicted by heat 6 which had the highest slag Fe_xO level of 0.21%, but also had low ingot oxygen levels of <5-7 ppm.

No data are available on the effect of rare earth oxides on the activity of FeO in $CaF_2/CaO/La_2O_3$ slags. Therefore, any role La_2O_3 may have exerted on these contradictory data cannot be determined. It is also unfortunate that no slag analysis is available from heat 1 which possessed low ingot oxygen levels.

B. Effect of Slag Basicity on Ingot Oxygen Content

Slag basicity is often defined as the ratio of basic oxides to acidic oxides. A more precise definition would identify a "basic" slag as one where there is an excess of O^{-2} ions in the slag and an "acidic" slag where there is a deficiency of O^{-2} ions[28]. CaO and MgO are classified as basic in nature because they donate O^{-2} ions to the slag when they dissociate to form Ca^{+2} and Mg^{+2} cations and O^{-2} anions. SiO_2 is considered acidic because it accepts O^{-2} ions to form SiO_4^{-4} ions. Al_2O_3 is considered amphoteric because it can behave as either an acid or base. In the presence of CaO, Al_2O_3 will behave as an acid and form ions of AlO_3^{-3}.

Most commercial ESR slags contain significant amounts of CaO and Al_2O_3. CaO is beneficial because it possesses a very high negative free energy which enables Ca^{+2} ions to reduce chemically any other metal oxide except rare earth

oxides and consequently, favors low slag oxygen activities while maintaining good compositional control during ESR. CaO is also very basic. Al_2O_3 is added to ESR slags for its high electrical resistivity and because it possesses a relatively high negative free energy of formation as well. In most ESR applications, the presence of Al_2O_3 does not pose any problem to the refining capability of the slag. However, Al_2O_3 is also acidic in nature and may increase the oxygen activity of the slag. Duckworth and Hoyle[12] report that a 10% increase of Al_2O_3 in the slag increased the ingot oxygen content from 20 to 40 ppm in a ball-bearing steel.

The relationship between slag basicity and oxygen content in the steel is demonstrated in data reported by Jager[9] et al. in Figure 24. These data show how an increase in slag basicity lowers the oxygen content (a reflection of lower oxygen activity in the slag) of the alloy and lowers the oxide inclusion content. In Figure 24, basicity is defined as the CaO/SiO_2 ratio which obviously does not account for the contributions of all of the slag components.

"Optical basicity" is a recent refinement of the strict ratio method and accounts for the contributions of all major slag components to slag basicity[29-33]. The formula used to calculate optical basicity values for this study was that

derived by Duffy[29] and is given in Table XXIV. The literature contains optical basicity multiplication factors for many individual oxides and fluorides which are used in the calculation of a slag's optical basicity. However, no value can be found in the literature for La_2O_3 or CeO_2. Fortunately, Duffy and Ingram[34] have determined that the optical basicity of an oxide can be correlated to the Pauling electronegativity by the following formula:

$$\text{Mult. factor} = \frac{0.75}{x - 0.25}$$

where x equals the Pauling electronegativity. This equation was used to determine the multiplication factors for La_2O_3 and CeO_2 and happened to be 0.88 for both oxides. This value is not as high as that of CaO (1.0), but is higher than that of Al_2O_3 (0.60) and indicates that rare earth oxides are more basic than alumina.

Calculations of the optical basicities for all of the ESR slags used in this study were done and are listed in Table XXIV. The data show that the nominal $CaF_2/CaO/Al_2O_3$ slags used in this study had optical basicity values ranging from 0.598 to 0.617 while the ESR slags which substituted La_2O_3 for Al_2O_3 possessed significantly higher values of 0.683 and 0.685. The apparent effect of optical basicity on the

ESR ingot content can be observed quite well in the oxygen values of the ESR heats. Both heats melted with the La_2O_3 bearing slag - 5 and 6, possessed consistently low oxygen levels of approximately 5 ppm whereas the nominal CaF_2-CaO-Al_2O_3 heats contained oxygen levels ranging from 5-56 ppm.

The mechanism by which increased slag basicities may help lower the oxygen activity of the slag appears somewhat complex and may reflect the influence of more than one slag parameter. A change in the relative activities of various slag components could explain why La_2O_3 was able to lower the oxygen activity of the slag and therefore, the ingot. Hawkins and Davies[26] have clearly shown that the activity coefficient of FeO is lowered as the CaO content of a CaF_2/CaO/FeO slag is increased as graphed in Figure 25. As the activity coefficient of FeO is decreased, the activities of Fe and oxygen in the slag are lowered by a corresponding amount. Thus, because the oxygen content of the metal is dictated by the oxygen activity of the slag, lower slag oxygen activities should produce lower ingot oxygen values.

This understanding could provide further insight to the Figure 24 data generated by Jager[9] et al. It is clear that the increased basicity in Figure 24 was due to an increased CaO content which would have decreased the FeO and oxygen

activity. The exact composition of Jager's slag is unknown; however, it is likely to be a $CaF_2/CaO/Al_2O_3$ slag since most slags used to ESR superalloys are variations on this system.

With regard to the present study, it is quite possible that the substitution of La_2O_3 for Al_2O_3 may have lowered the activity of FeO. Unfortunately, no data are available in the literature as to the effect of La_2O_3 on the activity of FeO in $CaF_2/CaO/Al_2O_3$ slags. However, Hawkins and Davies[26] claimed in their work that the activity of FeO in the slag increased when up to 8% Al_2O_3 was added to a $CaF_2/CaO/FeO$ slag. Their work also clearly showed as graphed in Figure 25, that the activity coefficient of FeO in the $CaF_2/CaO/FeO$ system is lowered as the concentration of CaO increases. Thus, high CaO levels in the ESR slag should consequently help to lower the oxygen activity of the slag while increasing Al_2O_3 levels would be expected to increase the oxygen activity of the slag. It has not been experimentally determined how Al_2O_3 in the range of 25-30% affects the FeO activity in $CaF_2/CaO/FeO$ slags. However, if the identified effects of CaO and Al_2O_3 on the FeO activity coefficients continue to hold true at Al_2O_3 levels of 25-30%, then substitution of La_2O_3 for Al_2O_3 may help achieve lower FeO activity coefficients and lower ingot oxygen levels.

The substitution of a more basic oxide such as La_2O_3 for Al_2O_3 in the slag would work to lower the FeO activity coefficient and oxygen activity in the slag (like CaO) and explain the improved oxygen refining capacity of the $CaF_2/CaO/La_2O_3/Al_2O_3$ slag compared to $CaF_2/CaO/Al_2O_3$ slags. In this study, it was not possible to completely replace Al_2O_3 with La_2O_3 in the slag because a minimal amount of Al_2O_3 is required to maintain compositional control of the Ti and Al during ESR. For Alloy 718, the La_2O_3 bearing slag still contained 8% Al_2O_3. Nevertheless, the low ingot oxygen data of heats 5 and 6 indicate that La_2O_3-bearing slags achieved lower slag oxygen activities than other heats in the study which used only $CaF_2/CaO/Al_2O_3$ slags. Continuing with this line of reasoning, the slightly higher oxygen levels in heat 6 compared to heat 5 could be explained by the Al deoxidation additions made during ESR of the latter heat which could have raised the oxygen activity of the slag a slight amount. In addition, it does not appear that the Al deoxidation additions provided any benefit to slag deoxidation in this case.

Another oxide which may also increase the oxygen activity of the slag because of its multivalent nature is titanium oxide. Mitchell[1] has pointed out that Ti can exist in three different valence states in the slag; Ti^{+2}, Ti^{+3}, and Ti^{+4}. One reaction which occurs at the slag/air

interface is

$$(Ti_2O_3) + 1/2\ O_2(g) \rightarrow 2(TiO_2).$$

This reaction is similar to the FeO reaction at the slag/air interface which contributes to high slag oxygen activities. Thus, if the slag is not completely shrouded with argon, which is a possibility in the present study, slag oxygen activity levels could likely be increased in the presence of titanium oxide. Mitchell[35] et al. have also determined that for FeO contents ranging from 0.02 - 0.07% in $CaF_2/CaO/Al_2O_3/SiO_2$ slags, oxygen activity increased as SiO_2 content increased. Since TiO_x and SiO_2 may have acted to increase the slag oxygen activity, La_2O_3 may have also acted to decrease the activity of these oxides as well although data are not available to conclusively established this hypothesis.

The data of the present study show optical basicity can be viewed as a gauge of the ultimate ability of CaO and La_2O_3-bearing slags to remove oxygen from the melt during ESR. This relationship could reflect lower FeO activity coefficients in the presence of high CaO and La_2O_3 levels. However, the contribution of a high negative free energy of formation to low slag oxygen activities cannot be underestimated. CaO and La_2O_3 both exhibit very high

negative free energies of formation and demonstrate a high affinity for oxygen. It is questionable that a basic oxide with a moderate to low negative free energy of formation such as K_2O would demonstrate the same basicity/ingot oxygen content relationship as observed with CaO and La_2O_3. It is also probable that other basic oxides which possess high negative free energies of formation such as MgO and CeO_2 will also demonstrate the same basicity/ingot oxygen relationship observed in this study and that of Jager[9].

For ESR under air cover, maintenance of a low slag oxygen activity through use of a basic slag composed of CaO and La_2O_3 and an optimized slag deoxidation practice will enable the slag to approach its ultimate oxygen refining capability. However, if the slag deoxidation practice is not optimized, a higher than desired ingot oxygen value will result. ESR under argon cover may only require the use of CaO/La_2O_3 basic slags (no deoxidation procedure) since the primary source of external oxygen to the slag has been eliminated through the argon shrouding. This reasoning is confirmed in the present study by the higher optical basicities of the $CaF_2/CaO/La_2O_3/Al_2O_3$ slags and lower ingot oxygen levels compared to the lower optical basicities and higher ingot oxygen levels associated with the $CaF_2/CaO/Al_2O_3$ slags.

Sulfur removal in La_2O_3 bearing slags appears to be comparable to that of $CaF_2/CaO/Al_2O_3$ slags. Heats 5 and 6 report sulfur levels of 5-7 ppm while other ESR heats melted with $CaF_2/CaO/Al_2O_3$ slags under air and argon reported sulfur levels of <5 ppm to 0.002%. Rare earth sulfides and oxysulfides possess high negative free energies of formation which are comparable to those of rare earth oxides[36,37]. Thus, rare earth oxide bearing slags should remove sulfur quite effectively during ESR as the data of this study show.

C. Effect of Slag Oxide Stability on Slag Oxygen Activity

In the attempt to improve the oxygen refining capability of the ESR slag to the highest possible level, it is important to consider the effect of all slag components to the oxygen activity of the slag. Duckworth and Hoyle[12] have stated that the oxygen content in the ESR ingot is directly related to the square root of the oxygen activity in the slag. Thus, while the oxygen activity of the slag is greatly influenced by slag/air oxidation reactions, slags composed of oxides with high negative free energies of formation are also essential to produce the lowest possible slag oxygen activity. An oxide with a large negative ΔG° will also have a large equilibrium constant (K_p) and have a low partial pressure of oxygen in the slag and consequently

in the metal as well. Thus, if the slag composition is adjusted to contain oxides with the largest ΔG° values, the ability to attain the lowest possible slag oxygen activity will be enhanced.

In this study, La_2O_3 was substituted for Al_2O_3 in the slag because La_2O_3 had a higher negative free energy of formation value than Al_2O_3. A comparison[37,38] of free energy of formation values at 1650C shows Al_2O_3 to have a value of approximately -700 kJ/mol O_2 and La_2O_3 a value of -800 kJ/mol O_2. The ESR ingot oxygen data show that the La_2O_3 bearing slags produced heats containing lower oxygen values than those containing Al_2O_3. These data indicate that the substitution of La_2O_3 for Al_2O_3 in the slag did indeed help achieve lower slag oxygen activities and ingot oxygen levels.

D. Effect of Argon Shrouding on Slag Oxygen Activity

The oxygen partial pressure above the ESR slag is an important variable in the ESR process because of the oxidation reactions which occur between the slag and atmosphere. The effect of argon shrouding is to reduce or eliminate these slag/atmosphere oxidation reactions. Previous work[7] in argon ESR of superalloys showed that one of the primary benefits of argon shrouding was that the slag

became a closed system where slag reactions became interdependent and more controllable due to the elimination of the slag/atmosphere reactions. This interdependence in turn enables reactive elements such as Ti and Al to be controlled in better fashion during ESR as compared to ESR under air. It is possible to maintain acceptable compositional control of superalloys containing Ti and Al during ESR under an air cover; however, this requires close control over slag composition and deoxidation practice.

Figure 26 shows the effect of oxygen content above the slag and the dissolved oxygen content in an electroslag remelted nickel-base alloy[9]. These data clearly show how the oxygen content of the ESR ingot is reduced as the oxygen potential above the slag is also lowered through shrouding with inert gas. This graph shows that an oxygen potential of 0.2% is the level required to maintain ingot oxygen contents to the lowest possible levels (for Figure 26 - 15 ppm). From a practical standpoint, the ability to maintain consistently the oxygen partial pressure above the slag at a low value is a considerable challenge due to the design of the furnace crucible and the convective air currents that are present above the slag. During ESR in this study, argon flow rates to the furnace chamber had to be continually increased throughout ESR in order to maintain oxygen partial pressures at levels of 2% or less.

One drawback of argon shrouding is the potential effect on sulfur removal during ESR. In ESR with an air cover, sulfur is passed from the slag into the atmosphere by the following reaction:

$$(S) + O_2(g) \rightarrow SO_2(g)$$

This reaction allows the slag to continually desulfurize during ESR and allows maximum desulfurization of the metal to occur. When an argon shroud over the slag is utilized, atmospheric oxygen is unavailable to the sulfur in the slag and SO_2 formation does not occur. As a result, sulfur removal during ESR is determined solely by the sulfur capacity of the slag. For electrodes of relatively low sulfur level, removal of sulfur during ESR is not adversely affected. For electrodes containing higher sulfur levels though, sulfur removal will probably be adequate in the beginning of ESR when the slag has not reached the sulfur saturation level. As ESR continues and the slag becomes saturated with sulfur, sulfur removal from the metal will cease. In this study, sulfur removal was adequate in both air and argon ESR heats. Sulfur levels were lowered by ESR by an average of 50%.

E. Relationship Between Slag Basicity and Slag Oxygen Activity

The relationship between slag oxygen activity and slag basicity and their effect on ingot oxygen content is not entirely clear. Data by Jager[9] in Figure 24 indicate that as slag basicity increases, the oxygen activity of the slag decreases and lowers the amount of oxygen retained in the ingot. No information was available in Jager's publication as to the slag composition(s) used to generate these data. If slag basicity alone dictated the oxygen activity of the slag, this would suggest that other basic oxides such as K_2O and Na_2O would be very effective oxides in ESR slags formulated to produce low oxygen ESR ingots. However, the low negative free energies of formation for K_2O and Na_2O make them unsuitable for ESR because most elements in the ingot would chemically reduce these oxides and make compositional control during ESR very difficult. BaO, which is also very basic, but contains a higher negative free energy of formation offers promise as another oxide that may enable very low ingot oxygen values to be attained during ESR. Unfortunately, BaO is both toxic and subject to strict environmental regulations, and for these reasons cannot be realistically pursued as an ESR slag component.

It is probable that in order to attain very low ESR

ingot oxygen contents that high basicity, low FeO activity, argon shrouding, and high negative free energies of formation are required simultaneously of the slag components. In fact, it is quite possible that high basicity promoted low ingot oxygen levels only because CaO and La_2O_3 possessed high negative free energies of formation and lowered the FeO activity in the slags. This reasoning would explain why La_2O_3-bearing slags obtained lower ESR ingot oxygen values than Al_2O_3-bearing slags. La_2O_3 had both a higher negative free energy of formation and optical basicity compared to Al_2O_3 and would support this line of reasoning.

F. Proper Control of Ti and Al During ESR

One difficulty encountered during ESR of superalloys is the control of Ti and Al. These elements are more difficult to control than most other elements because they both possess high negative free energies of formation of oxides and as a result tends to reduce other oxides of lower negative free energy. Ti poses an additional problem because it is a multivalent oxide which can increase the oxygen potential of the slag much in the same manner as FeO.

In order to maintain the proper ingot Ti and Al values during ESR, the slag Al_2O_3 and TiO_2 levels must be in

chemical equilibrium with the Ti and Al contents in the ESR ingot being melted[2,15,39,40]. If the slag is not in equilibrium distribution with the Ti and Al levels, it will undergo the proper oxidizing or reducing chemical reactions to bring it into equilibrium. To control Ti and Al, the reaction of importance is:

$$3[Ti] + 2(Al_2O_3) = 4[Al] + 3(TiO_2)$$

For Alloy 718 compositions containing nominally 1% Ti and 0.55% Al, the proper TiO_2 and Al_2O_3 slag contents should be as follows:

1. Argon ESR, $CaF_2/CaO/Al_2O_3$ slag: Al_2O_3 - 30.3%, TiO_2 - 4.10%
2. Argon ESR, $CaF_2/CaO/La_2O_3$ slag: Al_2O_3 - 8.0%, TiO_2 - 3.85%

An obvious example of the slag composition adjusting to reach an equilibrium concentration can be observed in heat 5. This was the first heat melted using La_2O_3 in the slag and there was no data available to estimate what the proper oxide ratios should be in the slag. Thus, it was recognized that compositional control would be compromised until a slag analysis could be performed on the slag from this heat. Ingot and slag analysis data from Tables V and IX, respectively, show that Al was oxidized from the ingot into the slag to form Al_2O_3. Since the argon shrouding made the

slag a closed system, TiO_2 was reduced as Al_2O_3 was oxidized and there was a corresponding increase of Ti in the ESR ingot as a result.

Slag analyses also indicate a loss of SiO_2 and MgO. A corresponding increase in Si is observed in the bottom of the ingot. However, no increase in Mg is recorded in the ESR ingot. The most likely explanation for the loss of Mg from both the slag and the ingot is that because Mg has both low solid solubility in 718 and a very high vapor pressure, it volatilized out of the slag into the atmosphere.

G. Effect of Slag Composition on Slag Electrical Conductivity

The use of an argon shroud over the slag versus an air shroud produced no discernable change to the electrical conductivity of the slag as evidenced by the similar current and voltage strip chart traces of air and argon melted heats. However, it appears that the addition of La_2O_3 to a $CaF_2/CaO/Al_2O_3$ slag at a level of 15-17% does significantly affect the electrical conductivity of the slag compared to $CaF_2/CaO/Al_2O_3$ slags containing 5% or less rare earth oxide. The need to operate the ESR furnace at slightly higher voltages for the La_2O_3-bearing slags indicates that their slag electrical resistivity was lower compared to that of

nominal $CaF_2/CaO/Al_2O_3$ slags. It is likely that, since La_2O_3 was added primarily at the expense of Al_2O_3, the lower electrical resistivity is more a reflection of less Al_2O_3 in the slag rather than a high La_2O_3 content. A principal reason Al_2O_3 is added to ESR slags is to raise their electrical resistivity to improve power efficiency. Therefore, slags with lower Al_2O_3 levels such as used in heats 5 and 6 would be expected to exhibit higher electrical conductivities compared to nominal $CaF_2/CaO/Al_2O_3$ slags.

H. Microstructural Analysis of ESR Ingots

A review of the quantitative image analysis oxide data and the representative photomicrographs of the various heats reveals that the sizes of the oxides in the ingots of this study are on the order of less than 1 micron diameter and are almost always contained as a seed within a carbide or nitride. The exception to this condition is heat 3 which contained oxides approaching 2 microns diameter in the general structure. The very small size of the inclusions indicates that these oxides precipitated upon solidification during ESR and do not represent oxides from the prior VIM operation.

Research work on ESR by Mitchell[11] has shown that one primary advantage of ESR is that large oxides from the initial melting operation are dissolved into the slag during ESR and do not pass through to the remelted ingot. VAR does remove some large oxides, but cannot assure that all large oxides are removed from the ingot and is inferior to ESR with respect to this aspect of refining. Oxides present in ESR ingots precipitate from solution upon solidification and are consequently very small as long as the oxygen activity of the slag is kept low. If the slag is not properly controlled and deoxidized, the risk of precipitating larger inclusions during solidification is possible as was observed in heat 3 of this study, which contained high oxygen levels and larger oxysulfides and phosphides[19]. When oxides are small and contained within carbides and nitrides, they exert no impact on the safety and fatigue life of superalloys and are basically a nonfactor in terms of material performance. Thus, a major benefit of ESR is the removal of large oxides from the initial primary melting operation by dissolution of these oxides into the slag (provided that the slag is properly deoxidized)..

The oxides observed and measured in this study represent the background oxide inclusion content of the ESR ingot. It is reasonable to expect to find a relationship between the measured oxygen content and the amount of oxide

present in the microstructure. Figure 27 shows a graph of average volume percent oxide plotted as a function of oxygen content for each ingot location. As the data show, there is a general increase in inclusion content as oxygen content increases. Thus, lower oxygen levels translate into smaller oxide inclusions. Since microstructural analysis shows that most oxides act as seeds for nitride and carbide precipitation, it is unknown if low oxygen levels can alter the carbide/nitride size and distribution in the microstructure by reducing the number of nucleation sites. However, it is likely that the local solidification time still plays the predominant role in determining the carbide/nitride size and distribution in the solidification microstructure.

Figure 28 shows a plot of average oxide area plotted as a function of average volume percent oxide for each location. These data also show a rather strong trend that as volume percent oxide decreases, oxide size also decreases. Table XI shows the melt rates for all the heats to vary between 210 to 295 lbs/h and ingot cooling conditions were similar for all six ingots. Thus, the heat extraction and local solidification times should be comparable for each of the ingots. These similar solidification conditions indicate that differences in oxide

size are probably the function of the oxygen level of the ingot.

Because oxides are contained within carbides and nitrides, the carbide/nitride distribution within the microstructure becomes the limiting factor in material safety and performance. Work[41,42] has shown that nitrides have a greater tendency to agglomerate into inclusion clusters than oxides. Thus future work should concentrate on control of nitrogen and nitride precipitation in the microstructure as a means to improve superalloy material performance.

I. Gleeble/Forged Bar Data Correlation

The forging behavior of heats 3 and 4 was unexpected based upon the Gleeble test data of the respective heats. The Gleeble test strain rate of 1/second and that of the open die press forging are within the same order of magnitude and consequently dismisses strain rate as a significant variable which could affect hot ductility. A microstructural examination of the heat 3 forged bar which demonstrated unexpected poor ductility was performed. Close examination of the crack root area showed that the fracture followed a grain boundary. Representative photomicrographs of the unetched and etched conditions are shown in

Figure 29. Inspection of the forged bar structure also revealed a very coarse grain structure with very few grain boundaries. Review of the heat 3 chemical composition shows that this heat retained the highest combined levels of Ce and La of the heats in the study.

Published literature[43-45] reveals that a small addition of a rare earth element to an alloy is beneficial to material cleanness and ductility; however, excessive amounts are deleterious to hot working and mechanical properties. Data have been published on nickel base superalloys such as 80Ni-20Cr, Inconel® 901 and Waspaloy®, but not on Alloy 718. Published data suggest that rare earth additions of approximately 0.02% provide the maximum benefit to hot workability and ductility, whereas the combined Ce and La levels in heat 3 ranged from 0.013% to a very high level of 0.059%. Ce has been found[45] to be more deleterious than La at higher levels because it tends to form a Ni_5Ce eutectic at the grain boundaries, whereas La does not form a eutectic but dissolves in the matrix more readily.

In the current study, it is likely that the high Ce and

Inconel® is a registered trademark of Inco family companies.

Waspaloy® is a registered trademark of United Technologies Corp.

La levels of heat 3 in combination with the very coarse as-cast grain size contributed to an excessively high concentration of rare earth elements in the grain boundaries, which consequently formed a low melting point eutectic phase. This phase liquified at the 2050F hot working temperature and led to the large forging tears which developed during initial hot working of the heat 3 ingot section. Thus, the forging behavior of heat 3 is consistent with the literature.

As to why the poor forging behavior of heat 3 was not reflected in the Gleeble data, there is only one reasonable explanation. As stated earlier, the as-cast grain size of heat 3 was very coarse. It is possible that the various 0.252" Gleeble specimens from heat 3 contained little and perhaps no grain boundary area in the tested cross sections. Thus, the Gleeble specimen data reflected the matrix ductility in the absence of the highly segregated, low strength grain boundary effect and demonstrated high ductility as a result. Heats 5 and 6 contained no Ce, but comparable levels of La to heat 3. The lower concentration of rare earth elements enabled these heats to be forged with only slight tearing and more closely reflected the Gleeble hot ductility. The good forging behavior of heat 4 in spite of the poor Gleeble data remains unexplained, but may reflect the influence of the columnar and equiaxed as-cast

coarse grain structure.

It is possible that the benefits of Ce and La could be better realized if a smaller grain size could be achieved in the as-cast ingot. A small as-cast grain size would reduce the concentration of rare earth elements in the grain boundaries and minimize the formation of low melting point eutectic phases.

CONCLUSIONS

1. Substitution of La_2O_3 for Al_2O_3 in a slag increases the optical basicity of the slag and helps to lower the oxygen activity of the slag. The low oxygen activity of the slag produces a correspondingly low oxygen content in the ingot after ESR. The two La_2O_3 bearing slags containing the highest basicity produced ingot oxygen levels averaging only 5 ppm.

2. Partial substitution of La_2O_3 for Al_2O_3 in the ESR slag contributed to lower oxygen levels in the remelted ingot and suggests that the higher negative free energy of formation of La_2O_3 helped produce a lower oxygen activity in the slag than could be attained with larger levels of Al_2O_3.

3. Data of the study indicate that as both slag basicity and the negative free energy formation of oxides in the slag are simultaneously maximized, such as with CaO and La_2O_3, the slag oxygen activity will decrease and correspondingly produce lower oxygen levels in the remelted ingot. Proper deoxidation of the slag during ESR must also be performed in order to realize the advantages of this beneficial combination.

4. No significant correlation was observed between the total Fe_xO percent level in the slag and the oxygen content of the alloy 718 ingot after ESR.

5. Argon shrouding of the slag during ESR improves control of slag reactions, and helps to lower the slag oxygen activity when combined with a high slag basicity and slag oxides possessing high negative free energies of formation.

6. La_2O_3-bearing ESR slags can maintain proper Ti and Al levels in the remelted Alloy 718 ingot provided a minimal amount of Al_2O_3 and TiO_2 remain in the slag to achieve chemical equilibrium during ESR.

7. The partial substitution of La_2O_3 for Al_2O_3 in the ESR slag decreased the electrical resistivity of the slag and required higher voltages during ESR.

8. Oxides observed in the remelted ingot were on the order of one micron diameter when proper deoxidation techniques were utilized during ESR. Improper deoxidation of the slag during ESR can lead to the precipitation of larger oxides in the remelted ingot.

9. Oxides observed in the remelted ingot were almost always contained as seeds within carbides and nitrides. Therefore,

small oxides precipitated in this manner exert no significant impact on the mechanical property performance of Alloy 718. Future work should focus on the elimination of carbide and nitride clusters from the Alloy 718 microstructure.

10. Data show that as the volume percent oxide in the microstructure decreases, average oxide size also decreases. Measured oxygen content and volume percent oxide demonstrated a weaker, but similar correlation.

11. Microstructural analysis and published literature suggest that a high concentration of Ce and La was present in the grain boundaries of ingots exposed to La_2O_3 bearing slags and mischmetal deoxidant additions. Subsequent forging of those heats showed variable forgeability due to the high levels of rare earth elements at grain boundaries and somewhat mitigates the beneficial use of La_2O_3 as a means to lower the ESR slag oxygen potential. A smaller as-cast grain size in the ingot would reduce the rare earth element concentration at the grain boundaries and should correspondingly improve forgability.

12. Gleeble hot ductility values demonstrated a mixed correlation to actual heat forgeability. It is believed that some Gleeble specimens demonstrated high ductility

during testing because the specimen cross section did not contain grain boundaries. Larger sections of material from the as cast ingot which did contain weakened grain boundaries demonstrated poorer hot ductility during actual forging trials.

REFERENCES

1. Mitchell, A., "Melting and Refining of Superalloys and Titanium Alloys," Iron and Steel Institute of Japan International, 1992, vol. 32 (5), pp. 557-562.

2. Choudhary, A., "State of the Art of Superalloy Production for Aerospace and Other Application Using VIM/VAR or VIM/ESR," Iron and Steel Institute of Japan International, 1992, vol. 32 (5), pp. 563-574.

3. Titanium Rotating Components Review Team Report, Federal Aviation Administration, United States of America, December 14, 1990.

4. Hoyle, G., Electroslag Processes - Principles and Practice, Applied Science Publishers, London, 1983, 215 pp.

5. Kay, D. A. R. and R. J. Pomfret, "Removal of Oxide Inclusions During AC Electroslag Remelting," Journal of the Iron and Steel Institute, 1971, vol. 209 (12) pp. 962-965.

6. Wadier, J. F., Y. Honnorat, and J. Morlet, "Process Study of the Increased Cleanness Arising From Consumable Electrode Remelting," Tool Alloy Steels, 1978, vol. 12 (4), pp. 127-136.

7. Wegman, D., "Investigation of Electroslag Remelting under an Argon Atmosphere and Resulting Effects on Compositional Control and Alloy Cleanliness," Carpenter Technology Corporation Internal Report, March 13, 1987.

8. Tommaney, J., P. S. Andolina, and R. C. Buri, "Method and Means of Reducing the Oxidization of Reactive Elements in an Electroslag Remelting Operation" United States Patent 4,953,177, August 28, 1990.

9. Jager, H., F. Koch, P. Cerwenka, and A. Kapfenberg, "Characteristics of the ESR and VAR Processes in the Production of High-Performance Nickel-Base Alloys," Fachberichte Huttenpraxis Metallweiterverarbeitung, 1987, vol. 25 (4), pp. 307-314.

10. Reyes-Carmona, F. and A. Mitchell, "Deoxidation of ESR Slags," Iron and Steel Institute of Japan International, 1992, vol. 32 (4), pp. 529-537.

11. Mitchell, A., "Oxide Inclusion Behavior During Consumable Electrode Remelting," Ironmaking and Steelmaking, 1974, vol. 1 (3), pp. 172-179.

12. Duckworth, W. E. and G. Hoyle, Electro-Slag Refining, Chapman and Hall, London, 1969, pp 178.

13. Cooper, C. K., D. Ghosh, D. A. R. Kay, and R. J. Pomfret, "ESR Reaction Sites," Electric Furnace Conference Proceedings, TMS-AIME, 1970, vol. 28, pp. 8-12.

14. Kor, G. J. W. and F. D. Richardson, "Sulfide Capacities of Basic Slags Containing Calcium Fluoride," Transactions of the Metallurgical Society of AIME, 1969, vol. 245, pp. 319-327.

15. Wegman, D. D., "Compositional Control and Oxide Inclusion Level Comparison of Pyromet 718 and A-286 Ingots Electroslag Remelted Under Air vs. Argon Atmosphere," Sixth International Symposium on Superalloys, TMS-AIME, 1988, pp. 427-436.

16. Franklin, A. G., "Comparison Between a Quantitative Microscope and Chemical Methods for Assessment of Non-Metallic Inclusions," Journal of the Iron and Steel Institute, 1969, vol. 207 (2), pp. 181-186.

17. Jonsson, S. and S. Malm, "A Study of Micro Inclusions in Stainless Steels Made by the CLU-Converter Process," Scandinavian Journal of Metallurgy, 1978, vol. 7 (1), pp. 18-25.

18. Lindon, P. H., "The Use of Image Analysis in Assessment of Growth and Separation of Deoxidation Products in Steel," Inter/Micro '67 Conference, Cambridge, England, 1967, pp. 137-150.

19. Hill, K. A., Carpenter Technology Internal SEM Report, February 22, 1993.

20. Kauffman, D., Carpenter Technology Metal Physics Report No. 88032, October 19, 1988.

21. Kauffman, D., Carpenter Technology Metal Physics Report No. 89335, August 24, 1989.

22. Kauffman, D., Carpenter Technology Internal Metal Physics Report No. 90305, March 23, 1990.

23. Kauffman, D., Carpenter Technology Internal Metal Physics Report No. 90307, April 5, 1990.

24. Kauffman, D., Carpenter Technology Internal Metal Physics Report No. 90324, August 8, 1990.

25. Christman, T., Carpenter Technology Internal Metal Physics Report 92-193, January 7, 1993.

26. Hawkins, R. J. and M. W. Davies, "Thermodynamics of FeO-Bearing CaF_2-Based Slags," Journal of the Iron and Steel Institute, 1971, vol. 209 (3), pp. 226-230.

27. Sasabe, M. and A. Asamura, "Transport Phenomenon of Oxygen Through Molten Slags," Second International Symposium on Metallurgical Slags and Fluxes, TMS-AIME, 1984, pp. 651-667.

28. Moore, J. J., Chemical Metallurgy, Butterworths, London, 1981, pp. 380.

29. Duffy, J., "Optical Basicity of Fluoride Containing Slags," Ironmaking and Steelmaking, 1990, vol. 17 (6), pp. 410-413.

30. Gaskell, D. R., "On the Correlation between the Distribution of Phosphorus between Slag and Metal and the Theoretical Optical Basicity of the Slag," Iron and Steel Institute of Japan, 1982, vol. 22 (12), pp. 997-1000.

31. Sommerville, I. D. and D. J. Sosinsky, "The Application of the Optical Basicity Concept to Metallurgical Slags," Second International Symposium on Metallurgical Slags and Fluxes, TMS-AIME, 1984, pp. 1015-1026.

32. Sosinsky, D. J. and I. D. Sommerville, "The Composition and Temperature Dependence of the Sulfide Capacity of Metallurgical Slags," Metallurgical Transactions B, 1986, vol. 17B (6), pp. 331-337.

33. Sommerville, I. D. and C. R. Masson, "Group Optical Basicities of Polymerized Anions in Slags", Metallurgical Transactions B, 1992, vol. 23B (4), pp. 227-229.

34. Duffy, J. A. and M. D. Ingram, "Optical Basicity IV: Influence of Electronegativity on the Lewis Basicity and Solvent Properties of Molten Oxyanion Salts and Glasses," Journal of Inorganic Nuclear Chemistry, 1975, vol. 37, pp. 1203-1206.

35. Mitchell, A., F. Reyes-Carmona, and E. Samuelsson, "The Deoxidation of Low-alloy Steel Ingots During ESR," Iron and Steel Institute of Japan, 1984, vol. 24 (7), pp. 547-556.

36. Bingel, C. J. and L. V. Scott, Electric Furnace Conference Proceedings, TMS-AIME, 1973, vol. 31, pp. 171-174.

37. Waudby, P. E., "Rare Earth Additions to Steel," International Metals Reviews, 1978, vol. 23 (2), pp. 74-98.

38. Luyckx, L. and J. R. Jackman, "Current Trends in the Use of Rare Earths in Steelmaking," Electric Furnace Conference Proceedings, TMS-AIME, 1973, vol. 31, pp. 175-181.

39. Pateisky, G., H. Biele, and H. J. Fleischer, "The Reactions of Titanium and Silicon with Al_2O_3-CaO-CaF_2 Slags in the ESR Process," Journal of Vacuum Science and Technology, 1972, vol. 9 (6), pp. 1318-1321.

40. Schwerdtfeger, K., W. Wepner, and G. Pateisky, "Modelling of Chemical Reactions Occurring During Electroslag Remelting: Oxidation of Titanium in Stainless Steel," Ironmaking and Steelmaking, 1978, vol. 5 (3), pp. 135-143.

41. Mitchell, A. and D. W. Tripp, "The Case for Low-Nitrogen Superalloys," Conference on Special Melting and Process Technologies, San Diego, 1988, pp. 147-153.

42. Mitchell, A., "Thermochemistry of Inclusions in Superalloys," Advanced Materials and Processing Techniques for Structural Applications, Paris, 1987, pp. 233-241.

43. Bailey, R. E., R. R. Shiring, and R. J. Anderson, "Effects of a Rare Earth Addition on Unitemp," Third International Symposium on Superalloys, TMS-AIME, 1976, pp. 109-118.

44. Rawson, J. D. W., "Effect of Temperature on Forgeability of Some Heat-Resistant Alloys," Conference on Reheating for Hot Working, ISI, 1967, pp. 65-69.

45. Cosandey, F., D. Li, F. Sczerzenie, and J. K. Tien, "The Effect of Cerium on High Temperature Tensile and Creep Behavior of a Superalloy," Metallurgical Transactions A, 1983, vol. 14A (4), pp. 611-621.

TABLE I

ALLOY 718 HEAT 1 CHEMICAL COMPOSITION
AIR-ESR HEAT REMELTED USING NOMINAL SLAG WITH Al DEOXIDATION ADDITIONS*

	Electrode		Ingot			
Element	X	A	X	C	B	A
C	0.051	0.049	0.056	0.050	0.050	0.050
Mn	0.11	0.11	0.12	0.11	0.11	0.10
Si	0.15	0.14	0.18	0.16	0.15	0.15
P	0.006	0.007	0.010	0.009	0.005	0.010
S	0.002	0.002	0.001	0.002	0.002	0.002
Cr	18.47	18.51	18.35	18.50	18.47	18.44
Ni	52.32	52.23	52.22	52.27	52.25	52.27
Mo	3.03	3.03	3.04	3.04	3.03	3.03
Cu	0.05	0.04	0.05	0.05	0.05	0.05
Co	0.29	0.29	0.29	0.29	0.29	0.29
V	0.04	0.04	0.09	0.04	0.04	0.04
Ti	0.98	0.97	0.95	0.95	0.99	1.10
Al	0.57	0.61	0.50	0.56	0.58	0.55
N	-	-	0.008	0.007	0.006	0.006
O(ppm)	<5	<5	13	<5	13	<5
B	0.0032	0.0034	0.0023	0.0033	0.0033	0.0039
Cb	5.27	5.29	5.35	5.30	5.31	5.31
Fe	Bal.	Bal.	Bal.	Bal.	Bal.	Bal.
Ca(ppm)	15	15	15	15	15	15
Mg(ppm)	51	43	13	11	13	17

* Heat melted under air with nominal slag + 6% TiO_2 + 15 gr Al/5 min.

All values weight percent unless noted.

TABLE II

ALLOY 718 HEAT 2 CHEMICAL COMPOSITION
ARGON-ESR HEAT REMELTED USING NOMINAL SLAG AND Al DEOXIDATION ADDITIONS*

	Electrode		Ingot					
Element	X	A	X	E	D	C	B	A
C	0.037	0.042	0.042	0.043	0.044	0.042	0.042	0.040
Mn	0.09	0.09	0.09	0.09	0.09	0.09	0.09	0.09
Si	0.17	0.17	0.24	0.20	0.18	0.24	0.20	0.17
P	0.007	0.005	0.013	0.010	0.012	0.011	0.014	0.012
S (ppm)	14	15	<5	<5	<5	<5	<5	7
Cr	18.60	18.67	18.58	18.60	18.66	18.55	18.64	18.54
Ni	52.59	52.50	52.36	52.49	52.44	52.47	52.46	52.18
Mo	3.03	3.03	3.04	3.03	3.02	3.04	3.03	3.01
Cu	0.04	0.04	0.04	0.04	0.04	0.04	0.04	0.04
Co	0.20	0.20	0.20	0.20	0.20	0.20	0.20	0.20
Ti	1.02	1.03	1.04	0.98	1.01	1.00	0.99	1.11
Al	0.54	0.54	0.51	0.55	0.57	0.51	0.55	0.54
N	0.009	0.007	0.007	0.008	0.008	0.008	0.008	0.007
O (ppm)	16	9	31	26	22	23	18	8
B	0.0031	0.0032	0.0035	0.0034	0.0036	0.0031	0.0038	0.0035
Cb	5.29	5.25	5.35	5.29	5.21	5.38	5.24	5.21
Ta	<0.01	<0.01	<0.01	<0.01	<0.01	<0.01	<0.01	<0.01
Fe	17.87	17.93	18.30	18.29	18.33	18.23	18.32	18.65
Ca (ppm)	<10	<10	<5	<5	<5	<5	<5	<5
Mg (ppm)	50	50	17	15	21	16	17	25

* Heat melted under argon with nominal slag + 4.5% TiO_2 + 4 gr Al deoxidation addition every 5 min.

All values are weight percent unless noted.

TABLE III

ALLOY 718 HEAT 3 CHEMICAL COMPOSITION
AIR-ESR HEAT REMELTED USING NOMINAL SLAG WITH AND MISCHMETAL DEOXIDATION ADDITIONS*

	Electrode		Ingot			
Element	X	A	X	C	B	A
C	0.041	0.040	0.045	0.041	0.041	0.041
Mn	0.09	0.09	0.10	0.09	0.09	0.09
Si	0.18	0.18	0.21	0.19	0.19	0.19
P	0.008	0.007	0.009	0.009	0.009	0.009
S	7 ppm	8 ppm	4 ppm	4 ppm	4 ppm	5 ppm
Cr	18.69	18.78	18.66	18.72	18.76	18.69
Ni	52.45	52.52	52.36	52.44	52.42	52.43
Mo	3.03	3.00	3.03	3.02	3.01	3.02
Cu	0.04	0.04	0.04	0.04	0.04	0.04
Co	0.20	0.20	0.20	0.20	0.20	0.20
Ti	1.04	1.02	1.00	1.01	1.00	1.14
Al	0.57	0.60	0.53	0.62	0.65	0.55
N	0.008	0.008	0.008	0.008	0.009	0.008
O	36 ppm	31 ppm	54 ppm	56 ppm	46 ppm	40 ppm
B	0.0038	0.0035	0.0025	0.0033	0.0033	0.0032
Cb	5.32	5.11	5.36	5.26	5.24	5.33
Ta	0.03	0.03	0.04	0.03	0.03	0.03
Fe	18.11	18.19	18.20	18.13	18.11	18.05
Ca	<10 ppm	<10 ppm	<10 ppm	<10 ppm	<10 ppm	<10 ppm
Mg	50 ppm	60 ppm	20 ppm	25 ppm	25 ppm	35 ppm
Ce	10 ppm	<10 ppm	200 ppm	100 ppm	90 ppm	390 ppm
La	<3 ppm	<3 ppm	90 ppm	60 ppm	40 ppm	200 ppm

* Heat melted under argon cover using 35% CaF_2/28% CaO/2.9% MgO/28% Al_2O_3/3.3% TiO_2 slag.

All values are weight percent unless noted.

TABLE IV

ALLOY 718 VAR HEAT 4 CHEMICAL COMPOSITION

	Ingot			
Element	X	C	B	A
C	0.041	0.040	0.040	0.042
Mn	0.09	0.09	0.09	0.09
Si	0.17	0.16	0.16	0.17
P	0.007	0.007	0.007	0.007
S (ppm)	10	11	11	10
Cr	18.69	18.77	18.77	18.78
Ni	52.46	52.46	52.45	52.45
Mo	3.05	3.04	3.03	3.04
Cu	0.04	0.04	0.04	0.04
Co	0.20	0.20	0.20	0.20
V	0.06	0.06	0.06	0.06
Ti	1.04	1.02	1.02	1.02
Al	0.58	0.57	0.59	0.57
N	0.013	0.010	0.010	0.010
O (ppm)	<5	20	22	59
B	0.0038	0.0035	0.0040	0.0035
Cb	5.34	5.24	5.22	5.24
Ca (ppm)	<5	<5	<5	<5
Mg (ppm)	11	9	10	15

All values weight percent unless noted.

TABLE V

ALLOY 718 HEAT 5 CHEMICAL COMPOSITION
ARGON-ESR HEAT REMELTED WITH La_2O_3 BEARING SLAG*

	Electrode		Ingot			
Element	X	A	X	C	B	A
C	0.042	0.043	0.044	0.043	0.041	0.041
Mn	0.09	0.09	0.09	0.09	0.09	0.09
Si	0.17	0.17	0.24	0.21	0.17	0.17
P	0.008	0.007	0.010	0.009	0.008	0.009
S	12 ppm	12 ppm	6 ppm	6 ppm	6 ppm	6 ppm
Cr	18.76	18.79	18.73	18.74	18.78	18.75
Ni	52.38	52.46	52.40	52.45	52.41	52.43
Mo	3.02	3.00	3.03	3.02	3.02	3.01
Cu	0.04	0.04	0.04	0.04	0.04	0.04
Co	0.20	0.20	0.20	0.20	0.20	0.20
V	0.06	0.06	0.06	0.06	0.06	0.06
Ti	1.02	1.00	1.10	1.07	1.03	1.08
Al	0.58	0.60	0.33	0.42	0.51	0.50
N	0.007	0.009	0.006	0.010	0.009	0.009
O	<5 ppm	12 ppm	<5/6 ppm	<5/<5 ppm	<5/5 ppm	<5/5 ppm
B	0.0037	0.0034	0.0033	0.0033	0.0031	0.0037
Cb	5.24	5.08	5.35	5.24	5.27	5.25
Ta	<0.01	<0.01	<0.01	<0.01	<0.01	<0.01
Fe	18.21	18.31	18.21	18.21	18.19	18.20
Ca	<5 ppm	<5 ppm	6 ppm	6 ppm	8 ppm	5 ppm
Mg	55 ppm	55 ppm	33 ppm	33 ppm	27 ppm	16 ppm
La	<0.001	<0.001	140 ppm	130 ppm	180 ppm	100 ppm
Ce	<0.001	<0.001	<0.001	<0.001	<0.001	<0.001

* Heat melted under argon cover using 31% CaF_2/17.5% La_2O_3/ 32.5% CaO/8% MgO/3.75% TiO_2/2% SiO_2 slag.

All values are weight percent unless noted.

TABLE VI

ALLOY 718 HEAT 6 CHEMICAL COMPOSITION
ARGON-ESR HEAT REMELTED WITH RE-BALANCED La_2O_3 BEARING SLAG*

	Electrode		Ingot			
Element	X	A	X	C	B	A
C	0.042	0.042	0.044	0.042	0.043	0.041
Mn	0.08	0.08	0.09	0.09	0.09	0.09
Si	0.15	0.14	0.17	0.17	0.17	0.17
P	0.008	0.008	0.011	0.010	0.010	0.011
S	11 ppm	11 ppm	7 ppm	5 ppm	5 ppm	7 ppm
Cr	18.86	18.84	18.76	18.77	18.73	18.78
Ni	52.54	52.50	52.38	52.41	52.40	52.35
Mo	2.99	3.01	3.05	3.05	3.05	3.04
Cu	0.04	0.04	0.04	0.04	0.04	0.04
Co	0.20	0.20	0.20	0.20	0.20	0.20
V	0.06	0.06	0.06	0.06	0.06	0.06
Ti	0.98	0.99	0.94	0.95	1.00	1.04
Al	0.62	0.55	0.50	0.54	0.53	0.53
N	0.009	0.008	0.007	0.008	0.007	0.005
O	16 ppm	6 ppm	<5 ppm	7 ppm	5 ppm	6 ppm
B	-	0.0032	0.0032	0.0033	0.0037	0.0037
Cb	4.83	4.96	5.31	5.33	5.34	5.27
Fe	18.43	18.40	18.24	18.15	18.15	18.19
Ca	<10 ppm	<10 ppm	0.002	0.003	0.003	0.002
Mg	50 ppm	40 ppm	0.012	0.015	0.008	0.006
La	-	-	0.02	0.03	0.03	0.02

* Heat melted under argon cover using 32% CaF_2/16% La_2O_3/ 38% CaO/2.15% MgO/1.7% TiO_2/7.6% Al_2O_3 slag.

All values are weight percent unless noted.

TABLE VII

ALLOY 718 HEAT 2 SLAG COMPOSITIONS
AFTER ESR*

Slag Component	2X	2A
CaF_2	34.36	33.39
CaO	26.67	26.95
MgO	2.39	2.39
SiO_2	0.34	1.13
Al_2O_3	30.23	30.42
Fe_xO	0.09	0.11
Cr_2O_3	0.10	0.04
NiO	0.03	<0.01
MnO	<0.01	<0.01
TiO_2	4.35	3.79
ZnO	<0.01	<0.01
MoO_3	<0.01	<0.01
BaO	<0.01	<0.01
PbO	<0.01	<0.01
CoO	<0.01	<0.01
CuO	<0.01	<0.01
Na_2O	0.61	0.58

*2X represents slag from bottom half of ingot
2A represents slag from top half of ingot remelted after fuse failure

TABLE VIII

ALLOY 718 HEAT 3 SLAG COMPOSITIONS

Slag Component	Before ESR	After ESR
CaF_2	34.67	31.54
CaO	28.62	34.49
MgO	2.89	3.15
SiO_2	0.62	0.36
Al_2O_3	28.27	28.83
Fe_xO	0.13	0.09
Cr_2O_3	<0.01	0.25
NiO	0.03	0.03
CeO_2	<0.02	4.57
TiO_2	3.35	4.50
La_2O_3	<0.01	2.56
MoO_3	<0.01	<0.01
K_2O	<1.5	<1.5
PbO	<0.04	<0.04
CoO	<0.01	<0.01
CuO	<0.01	<0.01
Na_2O	<0.72	1.48

All values are weight percent.

TABLE IX

ALLOY 718 HEAT 5 SLAG COMPOSITIONS

Slag Component	Before ESR	After ESR
CaF_2	31.07	33.91
CaO	32.59	30.39
MgO	7.99	3.38
SiO_2	1.95	0.77
Al_2O_3	0.45	7.22
Fe_xO	0.16	0.03
Cr_2O_3	<0.01	0.03
NiO	0.01	0.05
MnO	<0.01	<0.01
TiO_2	3.75	1.87
ZnO	<0.01	<0.01
MoO_3	0.11	<0.01
BaO	<0.01	<0.01
PbO	<0.02	<0.02
CoO	0.01	0.01
CuO	<0.01	<0.01
Na_2O	0.07	<0.01
K_2O	0.04	<0.02
La_2O_3	17.47	17.36
CeO_2	0.05	0.06

All values are weight percent.

TABLE X

ALLOY 718 HEAT 6 SLAG COMPOSITIONS

Slag Component	Before ESR	After ESR
CaF_2	31.99	32.51
CaO	38.08	33.18
MgO	2.16	0.58
SiO_2	0.47	0.62
Al_2O_3	7.63	8.37
Fe_xO	0.10	0.21
Cr_2O_3	<0.01	0.18
NiO	0.03	0.42
MnO	<0.01	<0.01
TiO_2	1.67	3.85
ZnO	<0.01	<0.01
MoO_3	<0.01	0.05
BaO	<0.01	<0.01
PbO	<0.03	<0.05
CoO	<0.01	<0.01
CuO	<0.01	<0.01
La_2O_3	15.99	15.43

All values are weight percent.

TABLE XI

MELTING PARAMETERS FOR ALLOY 718 ESR REFINING STUDY

Heat	Melting Procedure	Steady State Voltage (V)	Steady State Current (kA)	Steady State Power (kW)	Total Melt Time (Min)	Avg. Melt Rate (Lb/H)	Pressure
1	ESR-AC Air Cover	25	3.4	115	76.2	222.4	760 mm
2	ESR-AC Argon Cover	25-30	3.2-3.4	110-115	100.7	210.3	760 mm
3	ESR-AC Argon Cover	28-30	3.4	105-112	92.0	227.6	760 mm
4	VAR-DC Vaccum	25	3.1	105	82.1	257.3	6-10 μm
5	ESR-AC Argon Cover	35-42	3.4	105-130	66.3	295.9	760 mm
6	ESR-AC Argon Cover	34	3.0	105	74.3	244.0	760 mm

TABLE XII

ALLOY 718 HEAT 1
QUANTITATIVE IMAGE ANALYSIS OXIDE INCLUSION DATA

Location	Oxygen Level (PPM)	V_V	N_A	$\bar{D}$	$\bar{A}$
A	<5	0.006±0.005	25.39±13.25	1.124	2.269
	..	0.004±0.003	26.80±12.23	1.320	1.601
	..	0.003±0.002	21.16±11.37	1.179	1.195
B	13	0.007±0.004	63.47±32.49	1.130	1.067
	..	0.007±0.004	76.16±36.31	0.971	0.939
	..	0.007±0.005	53.59±27.72	1.084	1.294
C	<5	0.004±0.003	39.49±16.24	0.911	0.928
	..	0.005±0.005	63.47±30.53	0.837	0.726
	..	0.003±0.002	53.59±16.09	0.813	0.623
X	13	0.004±0.002	56.42±18.01	0.819	0.695
	..	0.004±0.003	43.72±16.99	0.907	0.890
	..	0.005±0.003	64.88±16.86	0.848	0.815
Mean ($\bar{X}$)	8.5	0.0049	49.01	0.995	1.090
Standard Deviation (σ)	5.2	0.0015	17.70	0.167	0.462

V_V - volume %, ±95% confidence limit

N_A - No. of particles/mm^2, ±95% confidence limit

$\bar{D}$ - Average particle diameter, µm

$\bar{A}$ - Average particle area, μm^2

100 fields rated to generate each data point.

* - "D" slag + 6% TiO_2 + 15 gr Al/5 min. Deox Addition

TABLE XIII

ALLOY 718 HEAT 2
QUANTITATIVE IMAGE ANALYSIS OXIDE INCLUSION DATA

Location	Oxygen Level (PPM)	V_V	N_A	$\bar{D}$	$\bar{A}$
		0.003±0.001	35.94±11.42	0.822	0.722
A	8	0.001±0.001	21.16±8.02	0.681	0.658
		0.002±0.001	24.68±9.49	1.009	1.006
		0.004±0.002	57.12±14.55	0.954	0.779
B	18	0.004±0.001	64.88±14.90	0.740	0.563
		0.005±0.002	76.16±18.98	0.832	0.648
		0.004±0.002	48.66±12.33	1.009	0.924
C	23	0.005±0.002	57.83±16.88	0.870	0.819
		0.004±0.001	56.42±13.72	0.883	0.721
		0.005±0.002	57.83±14.16	0.992	0.901
D	22	0.005±0.002	57.12±14.55	0.955	0.846
		0.006±0.002	72.63±17.30	0.990	0.879
		0.004±0.001	61.35±15.62	0.915	0.687
E	26	0.003±0.001	74.04±16.96	0.632	0.409
		0.004±0.001	66.99±16.50	0.766	0.605
		0.003±0.001	41.61±11.05	0.892	0.797
X	31	0.003±0.001	35.26±10.69	0.868	0.810
		0.007±0.001	33.14±9.19	0.779	0.576
Mean ($\bar{X}$)	21.3	0.0037	52.38	0.866	0.742
Standard Deviation (σ)	7.8	0.0013	16.84	0.113	0.150

V_V - volume %, ±95% confidence limit

N_A - No. of particles/mm^2, ±95% confidence limit

$\bar{D}$ - Average particle diameter, µm

$\bar{A}$ - Average particle area, μm^2

TABLE XIV

ALLOY 718 HEAT 3
ARGON/ESR WITH MISCHMETAL DEOX ADDITION (25 gr/5 MIN)

Location	Oxygen Level (PPM)	V_V	N_A	$\bar{D}$	$\bar{A}$
		0.007±0.004	35.96±11.43	1.401	2.028
A	40	0.003±0.001	40.20±14.05	0.985	0.775
		0.008±0.006	26.80±10.44	1.439	2.840
		0.014±0.007	44.43±12.01	1.457	3.126
B	46	0.011±0.006	26.09±9.62	1.828	4.254
		0.023±0.014	38.08±11.38	1.942	6.136
		0.008±0.004	31.03±9.83	1.442	2.654
C	56	0.007±0.004	26.09±11.10	1.263	2.868
		0.009±0.004	28.21±9.99	1.812	3.202
		0.010±0.005	46.54±11.94	1.153	2.116
X	54	0.011±0.004	55.00±12.82	1.248	2.043
		0.010±0.004	62.06±14.35	1.209	1.579
Mean ($\bar{X}$)	49.0	0.010	38.37	1.431	2.802
Standard Deviation (σ)	7.4	0.0049	11.84	0.295	1.374

V_V - volume %, ±95% confidence limit

N_A - No. of particles/mm^2, ±95% confidence limit

$\bar{D}$ - Average particle diameter, μm

$\bar{A}$ - Average particle area, μm^2

200 fields rated to generate each data point.

TABLE XV

ALLOY 718 VAR HEAT 4
QUANTITATIVE IMAGE ANALYSIS OXIDE INCLUSION DATA

Location	Oxygen Level (PPM)	V_V	N_A	$\bar{D}$	$\bar{A}$
		0.002±0.001	26.09±9.41	0.802	0.732
A	59	0.002±0.001	24.68±9.49	0.890	0.641
		0.001±0.001	20.45±7.69	0.718	0.565
		0.002±0.001	12.69±7.38	1.109	1.439
B	22	0.001±0.001	21.86±9.82	0.849	0.677
		0.002±0.001	24.68±8.86	0.747	0.645
		0.001±0.001	14.10±6.20	0.923	0.827
C	20	0.002±0.001	26.79±9.48	0.884	0.810
		0.001±0.001	19.04±7.51	0.959	0.782
		0.001±0.001	16.92±6.94	0.968	0.865
X	<5	0.001±0.001	16.22±6.84	0.880	0.722
		0.003±0.003	23.98±10.01	0.978	1.146
Mean ($\bar{X}$)	26.3	0.0016	20.63	0.892	0.821
Standard Deviation (σ)	23.3	0.0007	4.81	0.108	0.245

V_V - volume %, ±95% confidence limit

N_A - No. of particles/mm^2, ±95% confidence limit

$\bar{D}$ - Average particle diameter, μm

$\bar{A}$ - Average particle area, μm^2

200 fields rated per data point.

TABLE XVI

ALLOY 718 ARGON-ESR WITH LANTHANIDE BEARING SLAG - HEAT 5
QUANTITATIVE IMAGE ANALYSIS OXIDE INCLUSION DATA

Location	Oxygen Level (PPM)	V_V	N_A	$\bar{D}$	$\bar{A}$
		0.002±0.001	31.03±11.45	0.667	0.546
A	<5/5	0.001±0.001	19.75±7.85	0.754	0.531
		0.002±0.001	21.86±11.77	0.870	0.789
		0.001±0.001	31.03±12.11	0.615	0.425
B	<5/5	0.002±0.001	42.31±12.39	0.669	0.395
		0.002±0.001	47.25±12.59	0.659	0.429
		0.001±0.001	28.21±10.37	0.579	0.373
C	<5/<5	0.001±0.001	11.28±5.67	0.948	0.820
		0.001±0.001	20.45±9.48	0.595	0.431
		0.002±0.001	36.67±11.80	0.771	0.573
X	<5/6	0.002±0.001	23.98±10.01	0.781	0.639
		0.002±0.001	24.68±9.88	0.951	0.881
Mean ($\bar{X}$)	<5	0.00158	28.21	0.738	0.569
Standard Deviation (σ)	0.4	0.00051	10.17	0.130	0.177

V_V - volume %, ±95% confidence limit

N_A - No. of particles/mm^2, ±95% confidence limit

$\bar{D}$ - Average particle diameter, μm

$\bar{A}$ - Average particle area, μm^2

200 fields rated to generate each data point.

TABLE XVII

ALLOY 718 ARGON-ESR WITH REBALANCED LANTHANIDE BEARING SLAG - HEAT 6
QUANTITATIVE IMAGE ANALYSIS OXIDE INCLUSION DATA

Location	Oxygen Level (PPM)	V_V	N_A	$\bar{D}$	$\bar{A}$
		0.007±0.002	60.45±13.36	1.081	1.081
A	6 PPM	0.004±0.001	87.44±16.58	0.738	0.508
		0.004±0.001	91.67±16.94	0 611	0.420
		0.006±0.002	86.74±16.36	0.801	0.638
B	5 PPM	0.005±0.001	137.51±21.42	0.539	0.335
		0.004±0.001	107.89±20.27	0.644	0.367
		0.003±0.001	60.65±14.73	0.675	0.561
C	7 PPM	0.002±0.001	72.63±15.43	0.509	0.247
		0.004±0.001	109.30±22.89	0.603	0.363
X	<5 PPM	0.005±0.002	60.65±14.86	0.959	0.892
Mean ($\bar{X}$)	5.5	0.0044	87.49	0.716	0.541
Standard Deviation (σ)	1.3	0.0014	25.40	0.184	0.265

V_V - volume %, ±95% confidence limit

N_A - No. of particles/mm^2, ±95% confidence limit

$\bar{D}$ - Average particle diameter, μm

$\bar{A}$ - Average particle area, μm^2

TABLE XVIII

ALLOY 718 ON-HEATING GLEEBLE DATA - HEAT #4 (VIM-VAR)

Test Temperature °F	U.T.S. (ksi)	R.A. (%)
1700	47.2	45.2
1800	47.5	32.8
1850	39.1	46.4
1875	32.8	35.7
1900	35.6	40.8
2000	13.1	16.0
2050	24.0	0
2100	20.2	0
2100	16.6	0

TABLE XIX

ALLOY 718 ON-HEATING AND ON-COOLING GLEEBLE DATA - HEAT #1

Test Type	Preheat Temperature (°F)	Test Temperature °F	UTS(ksi)	RA(%)
OH	2050	2050	24.3	70.6
OH	2050	2050	26.7	26.3
OH	2050	2050	21.3	14.4
OC	2050	1600	44.1	65.8
OC	2050	1600	41.5	59.8
OC	2050	1700	44.4	82.8
OC	2050	1700	43.7	80.9
OC	2050	1800	39.7	73.1
OC	2050	1800	42.9	80.4
OC	2050	1900	36.8	83.7
OC	2050	1900	33.0	81.9
OC	2050	2000	27.2	75.8
OC	2050	2000	24.3	80.1
OH	2000	2000	24.7	82.1
OH	2000	2000	25.5	81.5
OC	2000	1600	37.5	58.2
OC	2000	1700	40.1	70.5
OC	2000	1800	40.7	75.8
OC	2000	1900	41.1	58.0

OH = On Heating
OC = On Cooling

TABLE XX

ALLOY 718 ON-HEATING AND ON-COOLING GLEEBLE DATA - HEAT #3

Test Type	Preheat Temperature (°F)	Test Temperature °F	UTS(ksi)	RA(%)
OH	2050	2050	25.6	74.3
OH	2050	2050	25.2	72.4
OC	2050	1600	26.0	20.0
OC	2050	1600	41.7	60.0
OC	2050	1600	24.6	12.4
OC	2050	1700	41.9	71.9
OC	2050	1700	40.7	58.9
OC	2050	1700	37.3	38.3
OC	2050	1800	40.0	87.9
OC	2050	1800	40.5	90.1
OC	2050	1900	35.4	81.3
OC	2050	1900	33.4	82.8
OC	2050	2000	28.6	77.2
OC	2050	2000	28.6	80.2
OH	2000	2000	18.1	0
OH	2000	2000	77.4	0
OH	2000	2000	25.5	77.5
OC	2000	1700	43.7	80.5
OC	2000	1800	39.4	78.3
OC	2000	1900	35.6	87.1

OH = On Heating
OC = On Cooling

TABLE XXI

ALLOY 718 ON-COOLING GLEEBLE DATA* - HEAT #4

Test Type	Preheat Temperature (°F)	Test Temperature °F	UTS(ksi)	RA(%)
OC	2050	1600	48.6	32.3
OC	2050	1600	46.1	46.1
OC	2050	1700	50.5	40.4
OC	2050	1700	45.9	55.1
OC	2050	1800	44.9	43.2
OC	2050	1800	44.9	41.3
OC	2050	1900	35.6	37.8
OC	2050	1900	31.9	42.0
OC	2050	2000	28.7	10.9
OC	2050	2000	29.3	0
OC	2050	2000	27.6	47.8
OC	2000	1600	43.7	57.9
OC	2000	1600	44.1	34.7
OC	2000	1700	39.7	56.2
OC	2000	1700	38.7	35.0
OC	2000	1800	37.5	60.0
OC	2000	1800	48.8	31.3
OC	2000	1900	41.7	29.3
OC	2000	1900	33.3	50.0

OC = On Cooling

* On heating data for Heat 4 contained in Table XVIII

TABLE XXII

ALLOY 718 ON-HEATING AND ON-COOLING GLEEBLE DATA - HEAT #5

Test Type	Preheat Temperature (°F)	Test Temperature °F	UTS(ksi)	RA(%)
OH	2050	2050	20.9	13.2
OH	2050	2050	24.5	51.3
OH	2050	2050	25.3	46.0
OC	2050	1600	36.0	51.3
OC	2050	1600	38.4	52.2
OC	2050	1700	40.2	37.9
OC	2050	1700	37.7	48.6
OC	2050	1700	36.5	53.0
OC	2050	1800	37.4	39.5
OC	2050	1800	36.7	67.0
OC	2050	1800	41.7	53.8
OC	2050	1900	32.4	63.2
OC	2050	1900	28.6	66.4
OC	2050	2000	28.0	46.7
OC	2050	2000	30.9	30.1
OC	2050	2000	27.0	52.5
OH	2000	2000	26.4	39.2
OH	2000	2000	29.7	47.4
OC	2000	1700	41.1	56.5
OC	2000	1800	37.1	68.2
OC	2000	1900	36.7	42.6

OH = On Heating
OC = On Cooling

TABLE XXIII

ALLOY 718 ON-HEATING AND ON-COOLING GLEEBLE DATA - HEAT #6

Test Type	Preheat Temperature (°F)	Test Temperature °F	UTS(ksi)	RA(%)
OH	2050	2050	26.6	70.6
OH	2050	2050	26.3	68.8
OC	2050	1600	43.2	55.2
OC	2050	1600	44.5	54.0
OC	2050	1700	36.5	59.1
OC	2050	1700	40.4	60.1
OC	2050	1800	37.5	71.4
OC	2050	1800	38.4	72.3
OC	2050	1900	33.0	75.8
OC	2050	1900	32.6	76.6
OC	2050	2000	26.6	62.5
OC	2050	2000	27.4	60.5
OH	2000	2000	27.4	56.0
OH	2000	2000	29.0	60.6
OC	2000	1600	44.4	59.5
OC	2000	1700	42.2	62.3
OC	2000	1800	39.7	71.0
OC	2000	1900	27.9	70.9

OH = On Heating
OC = On Cooling

TABLE XXIV

OPTICAL BASICITY* VALUES OF ESR SLAGS
UTILIZED IN ALLOY 718 ESR STUDY

Heat #	Λ (Including CaF_2)	Λ (Excluding (CaF_2)
1†	0.598	0.687
2A	0.613	0.707
3	0.617	0.695
5	0.683	0.835
6	0.685	0.830

* Optical Basicity (Λ)

$$= \frac{aN_A\Lambda(A_xO_a) + bN_B\Lambda(B_xO_b + \ldots cN_c\Lambda(CF_c) + dN_D\Lambda(CF_D)}{aN_a + bN_B + \ldots cN_c + dN_D}$$

where

a,b,c,d = number of oxygen or fluoride atoms in the compound formula,

Λ = optical basicity value of the pure oxide or fluoride,

$N_{A,B,C,D}$ = mol or weight fraction of the compound within the slag. Weight percent oxide and fluoride values were used for calculation purposes in this study.

† - Estimated slag composition

A mol fraction would be 0.5; mol percent would be 50%. The term "mol or weight percent fraction" doesn't make sense.

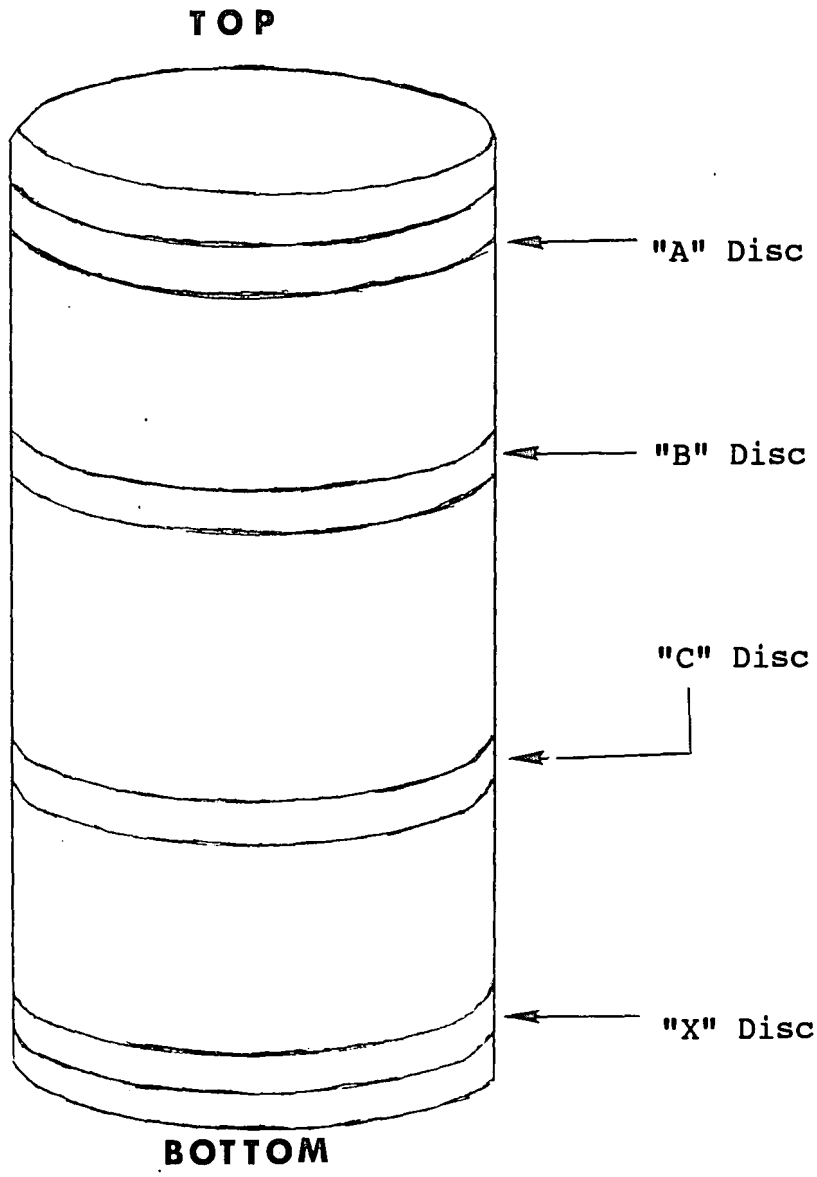

FIGURE 1 - Ingot Disc Locations for ESR Refining Study

GLEEBLE TEST SPECIMEN
.252

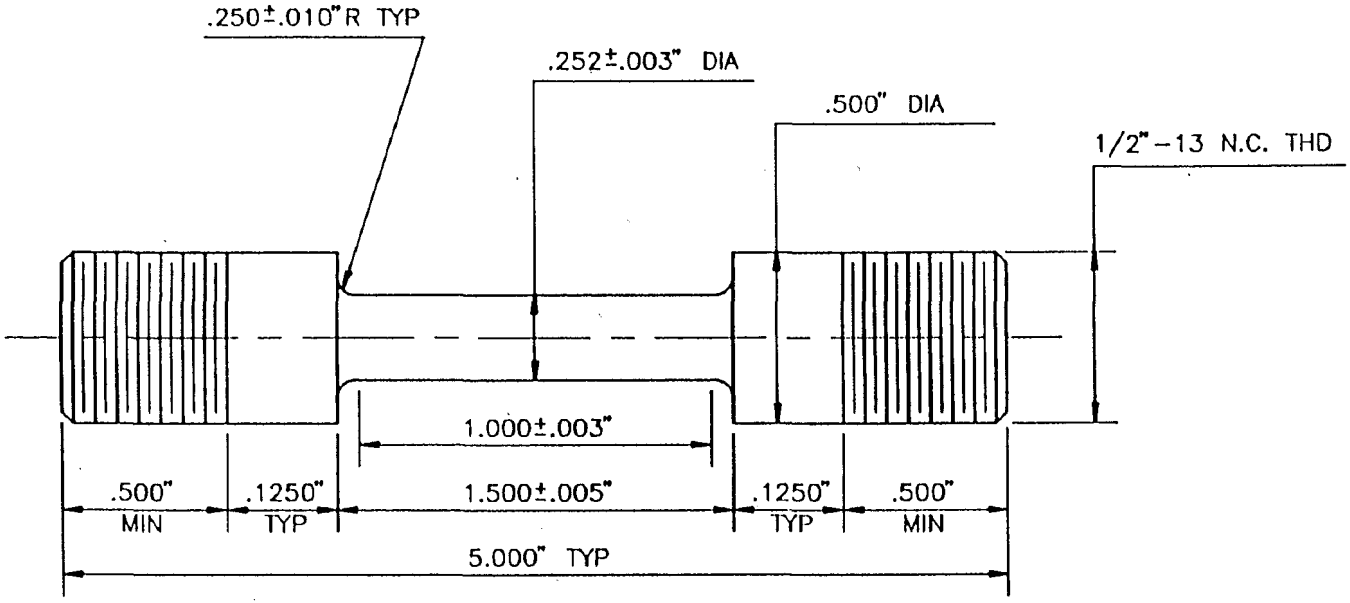

NOTE 1 A 320 GRIT POLISH WILL BE PROVIDED ON THE GAGE SECTION UNLESS SPECIFIED OTHERWISE.

FIGURE 2 - Gleeble Test Specimen (0.252") Used to Evaluate Hot Ductility of Various Heats Comprising ESR Refining Study

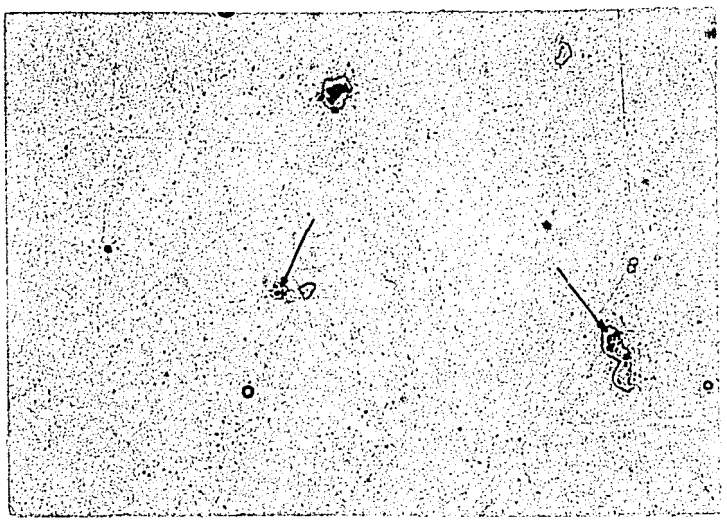

MAG: 400X **Etchant: None**

FIGURE 3 - Microstructure of Heat 1 - B Location. Note Carbides and Nitrides in Microstructure. Oxides are shown as seeds within carbides and nitrides.

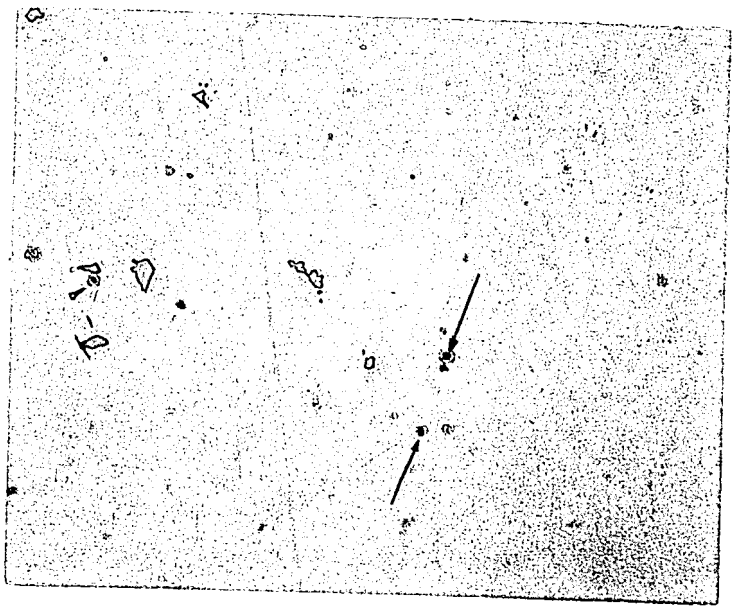

MAG: 400X **Etchant: None**

FIGURE 4 - Microstructure of Heat 2 - D Location. Note all oxides are contained within nitrides and carbides.

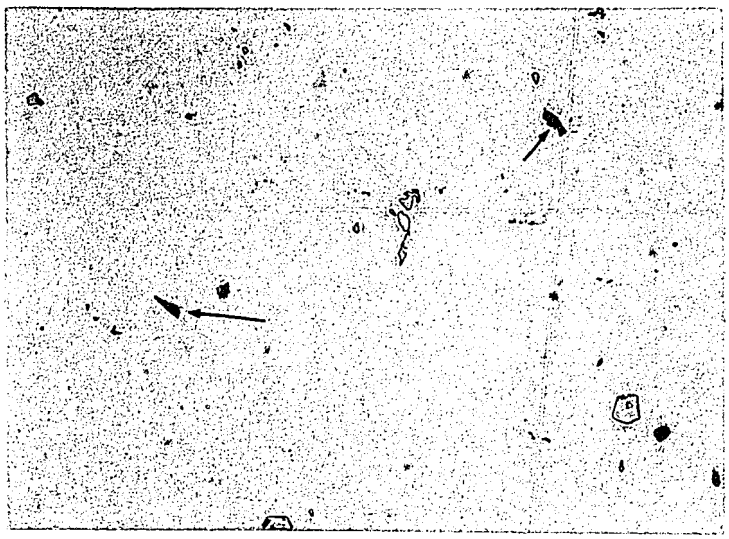

MAG: 400X **Etchant: None**

FIGURE 5 - Microstructure of Heat 3 - X Location. Note rare earth oxides in Microstructure. Oxides are not contained within carbides and nitrides.

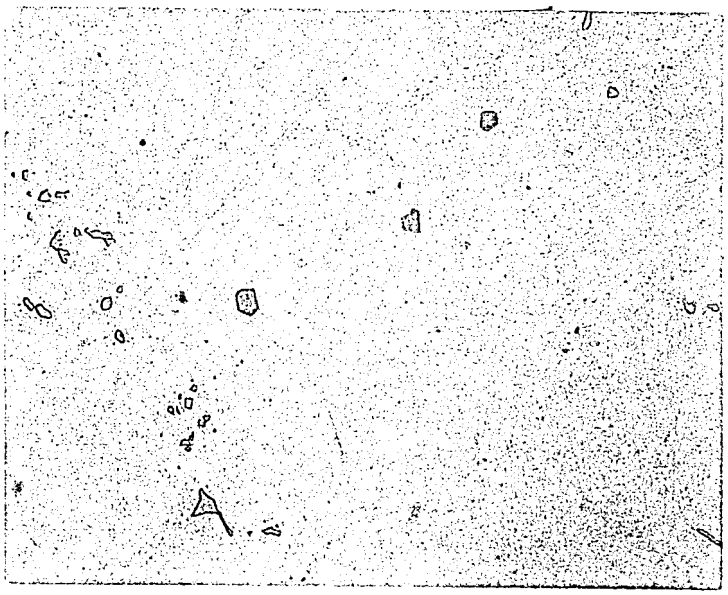

MAG: 400X **Etchant: None**

FIGURE 6 - Microstructure of Heat 4 - B Location. Very few oxides observed in microstructure.

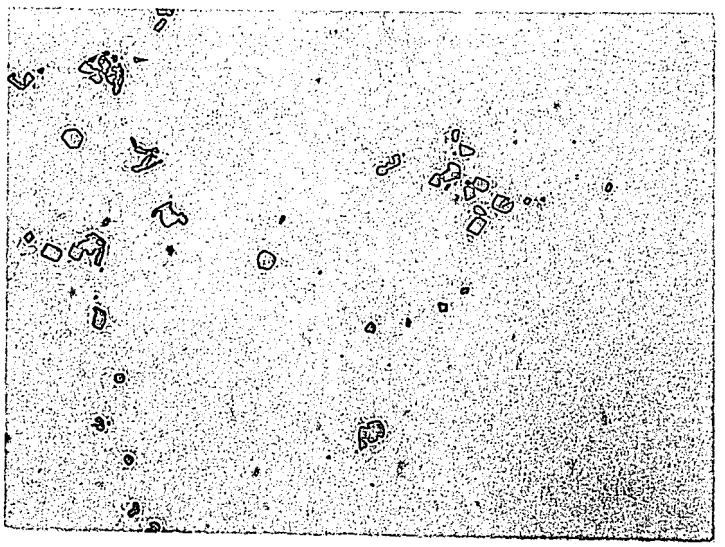

MAG: 400X Etchant: None

FIGURE 7 - Microstructure of Heat 5 - C Location. Virtually no oxides observed in microstructure.

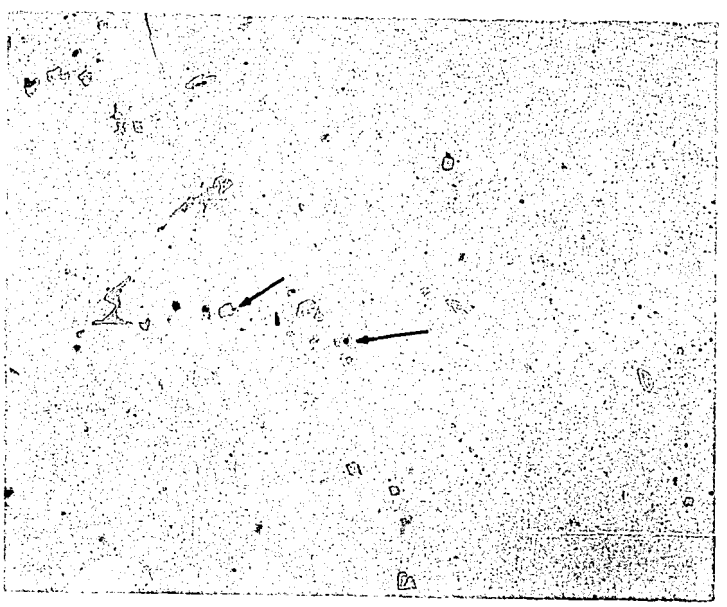

MAG: 400X Etchant: None

FIGURE 8 - Microstructure of Heat 6 - B Location. A few small oxides observed within carbides/nitrides and general microstructure.

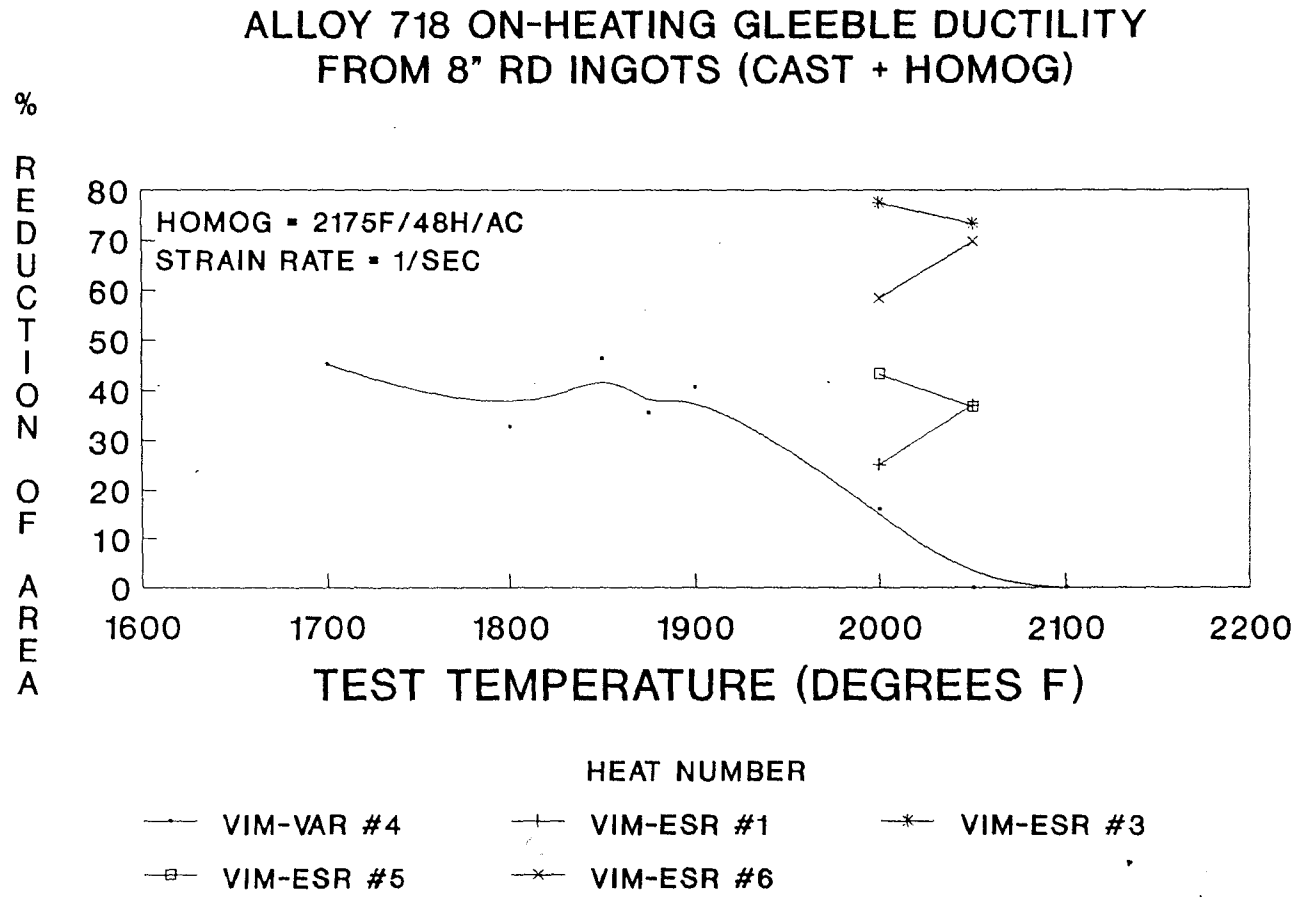

FIGURE 9 - Alloy 718 On-Heating Gleeble Data for ESR Refining Study

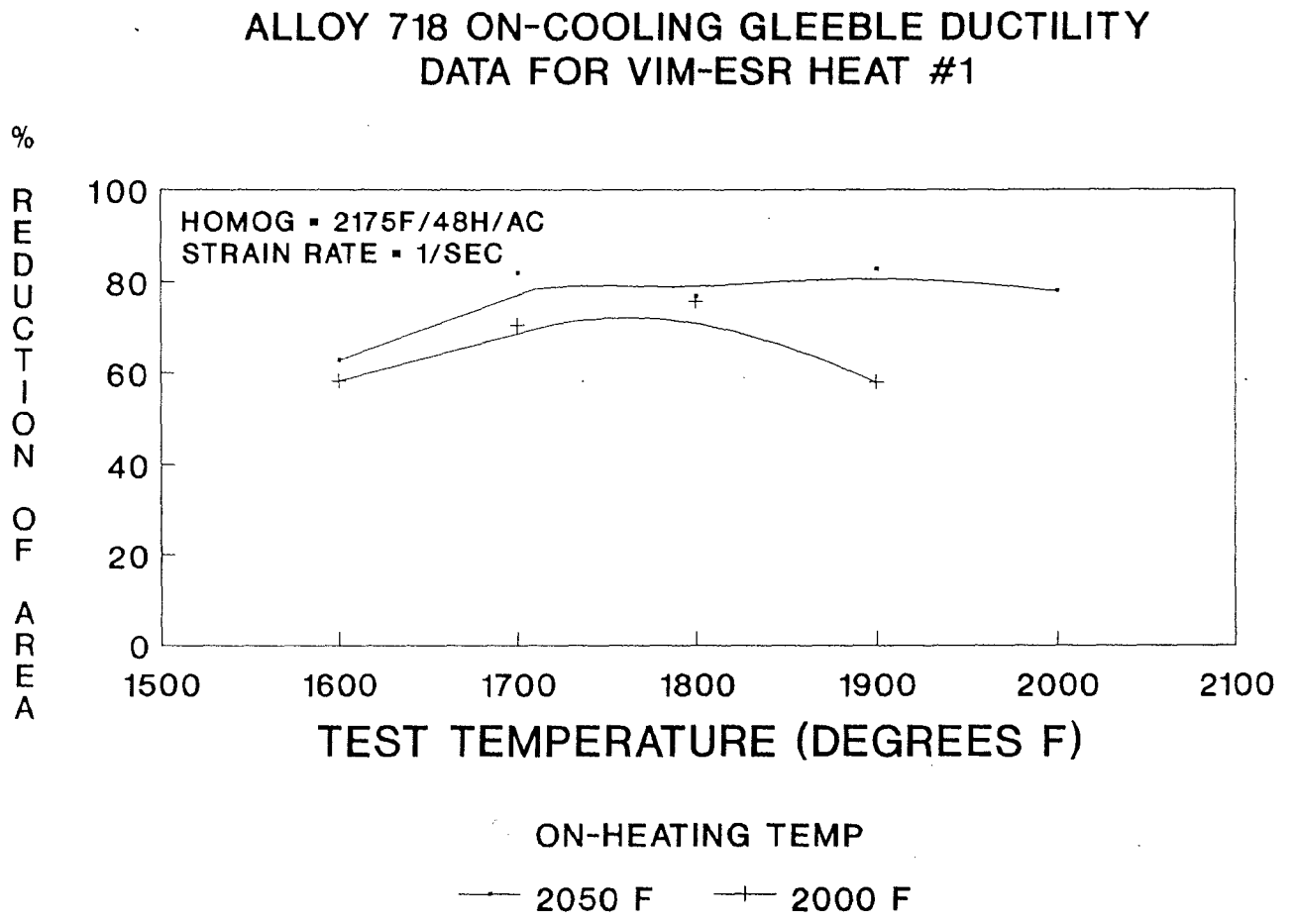

FIGURE 10 - Alloy 718 On-Cooling Gleeble Data from Heat 1 of ESR Refining Study

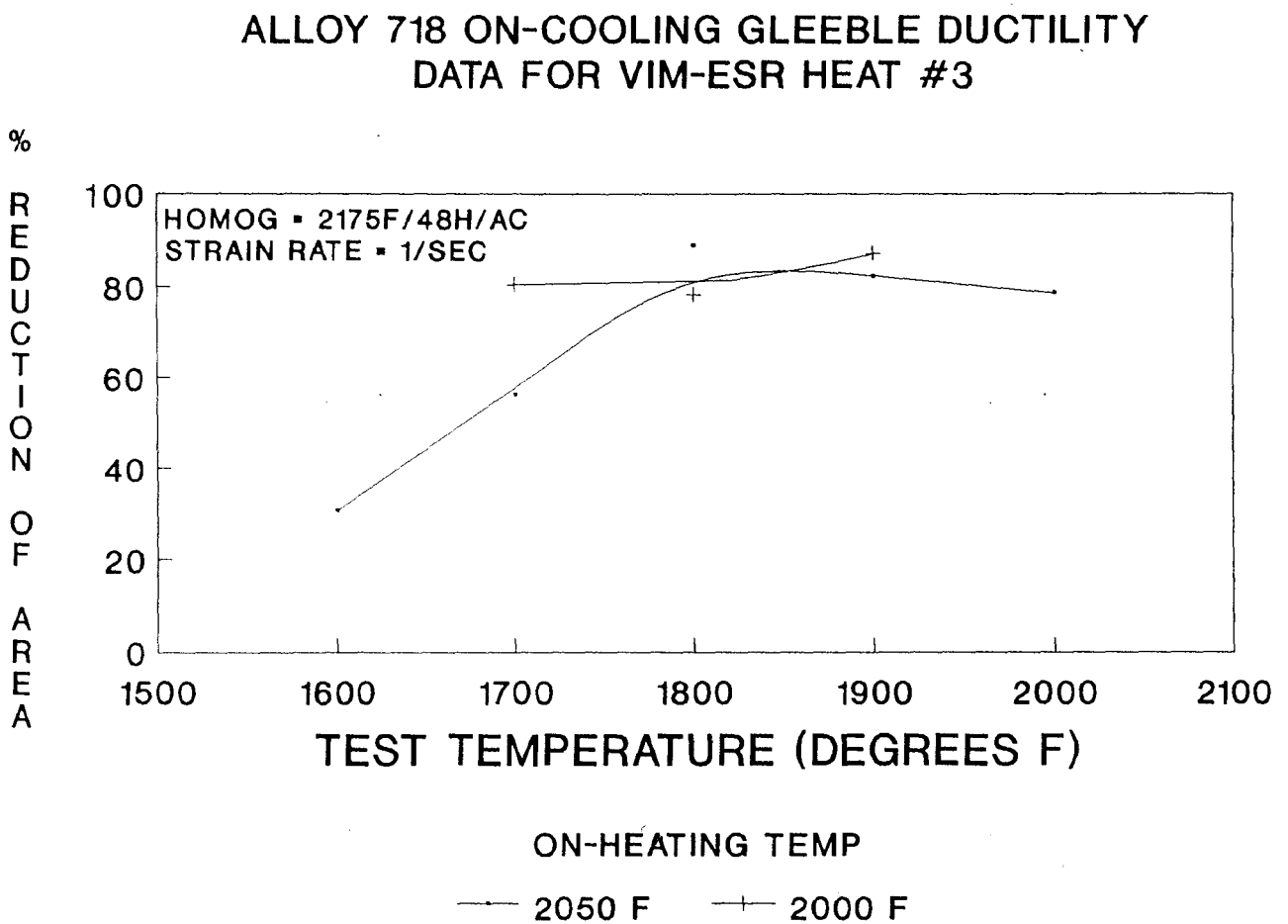

FIGURE 11 - Alloy 718 On-Cooling Gleeble Data from Heat 3 of ESR Refining Study

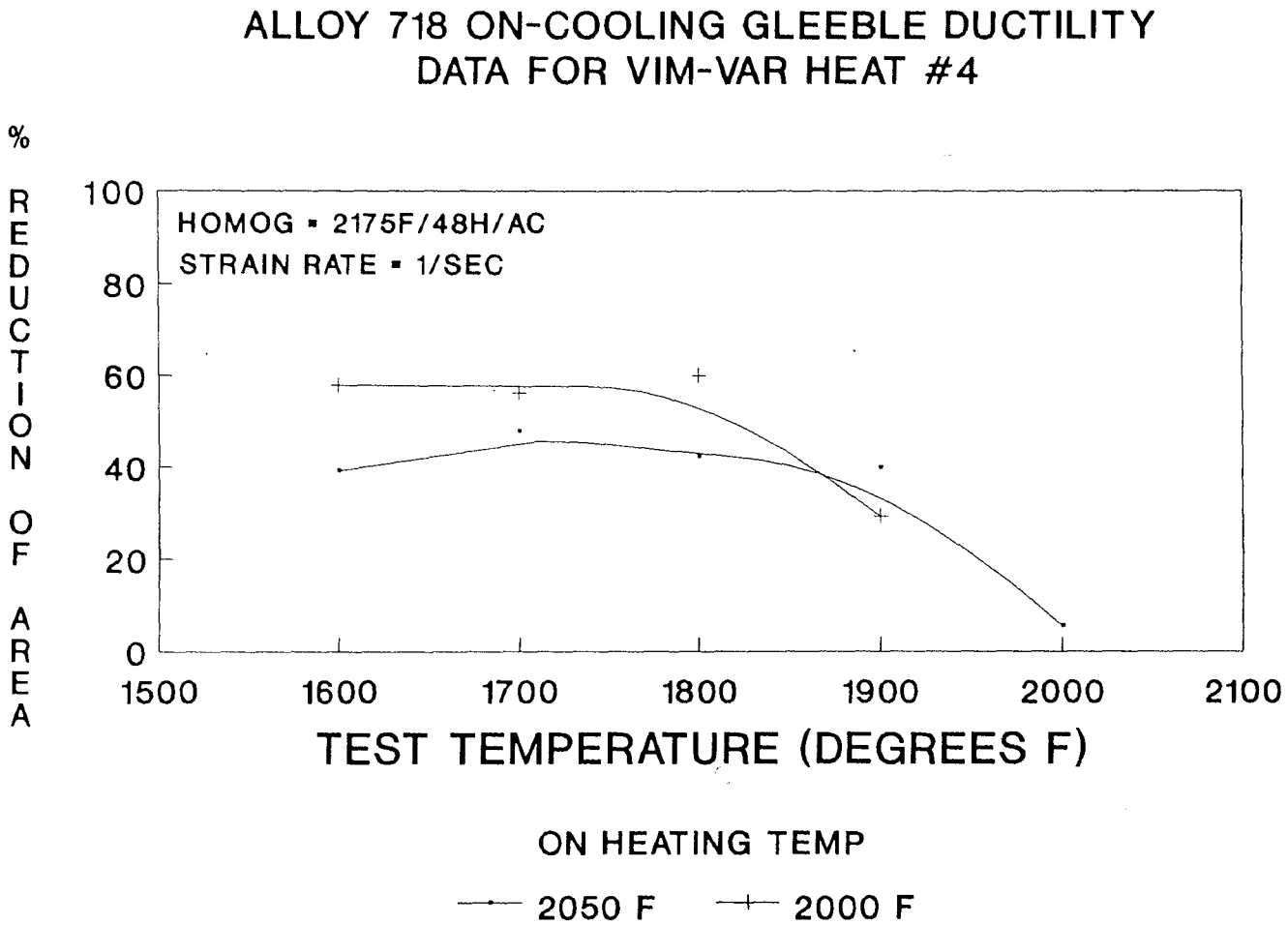

FIGURE 12 - Alloy 718 On-Cooling Gleeble Data from Heat 4 of ESR Refining Study

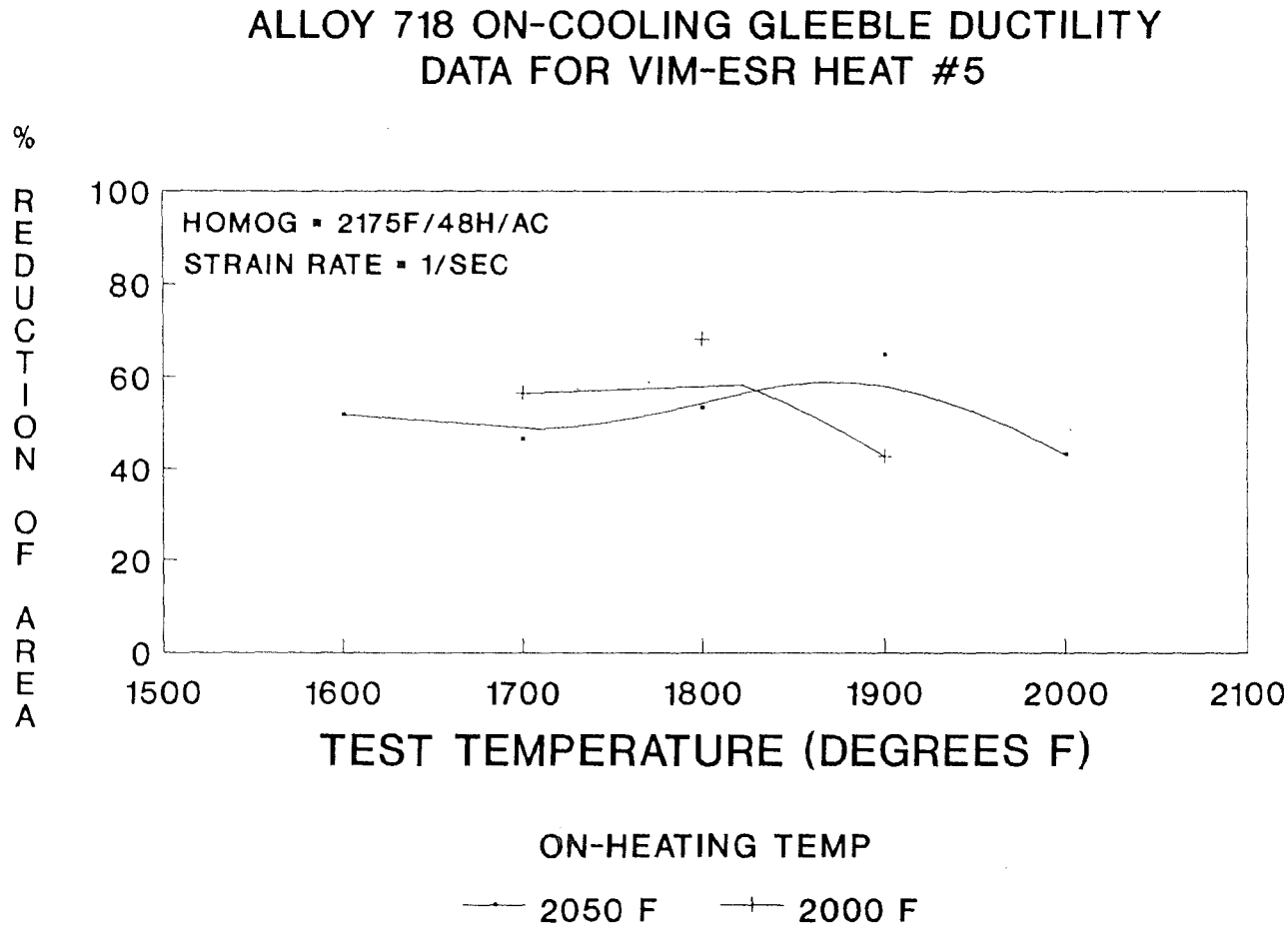

FIGURE 13 - Alloy 718 On-Cooling Gleeble Data for Heat 5 of ESR Refining Study

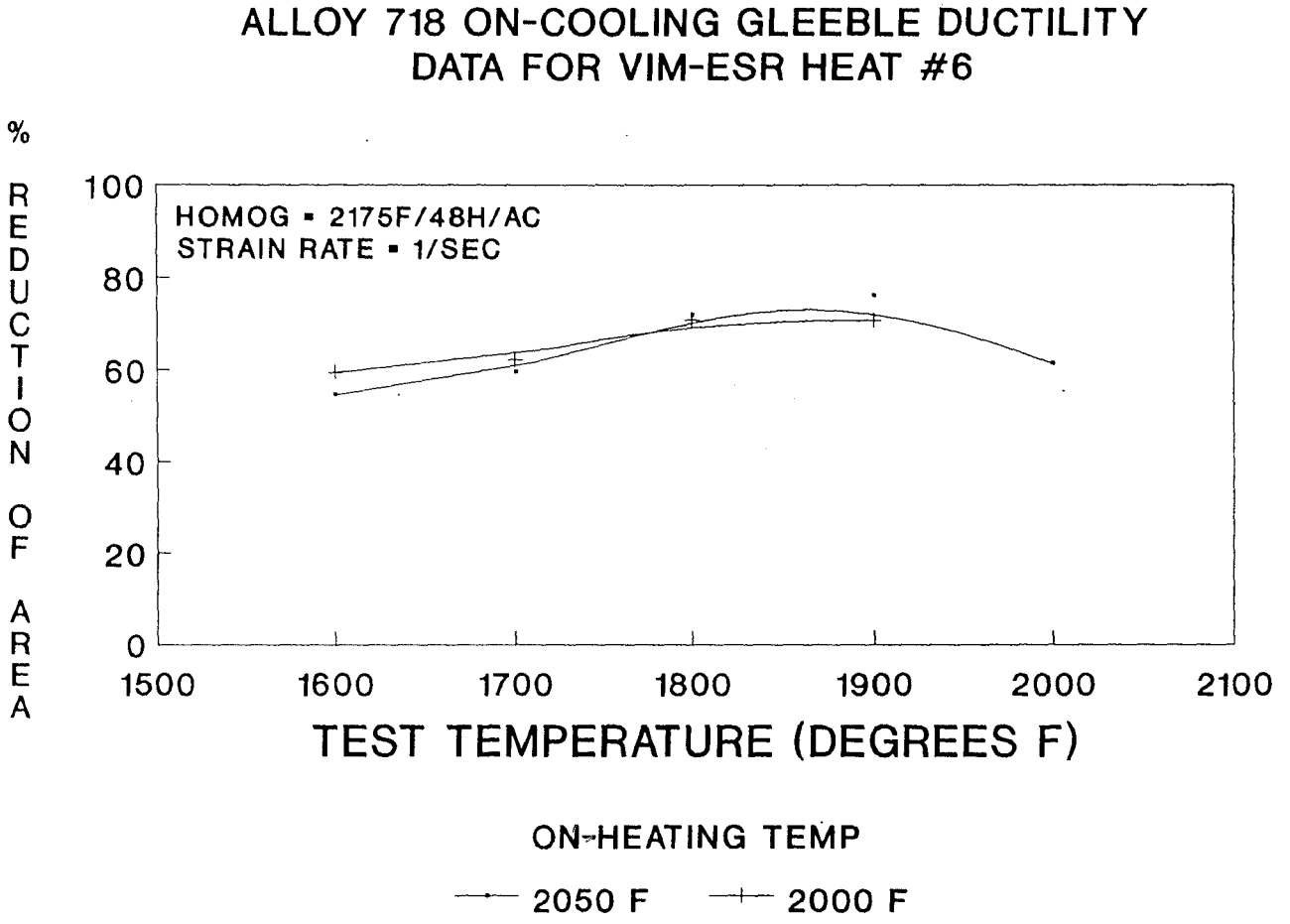

FIGURE 14 - Alloy 718 On-Cooling Gleeble Data for Heat 6 of ESR Refining Study

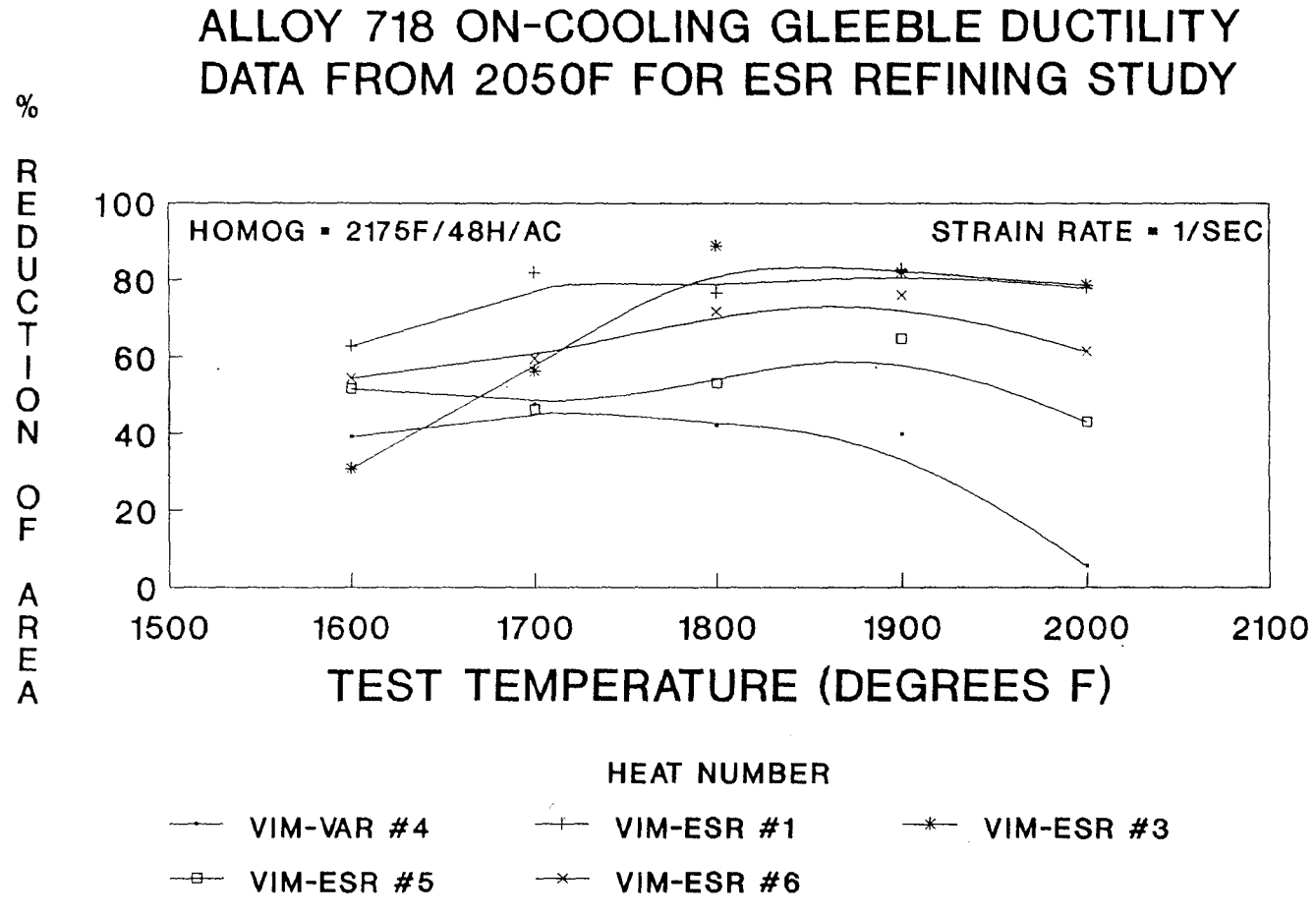

FIGURE 15 - **Composite of All Alloy 718 On-Cooling Gleeble Data from Pre-Heat Temperature of 2050F for ESR Refining Study**

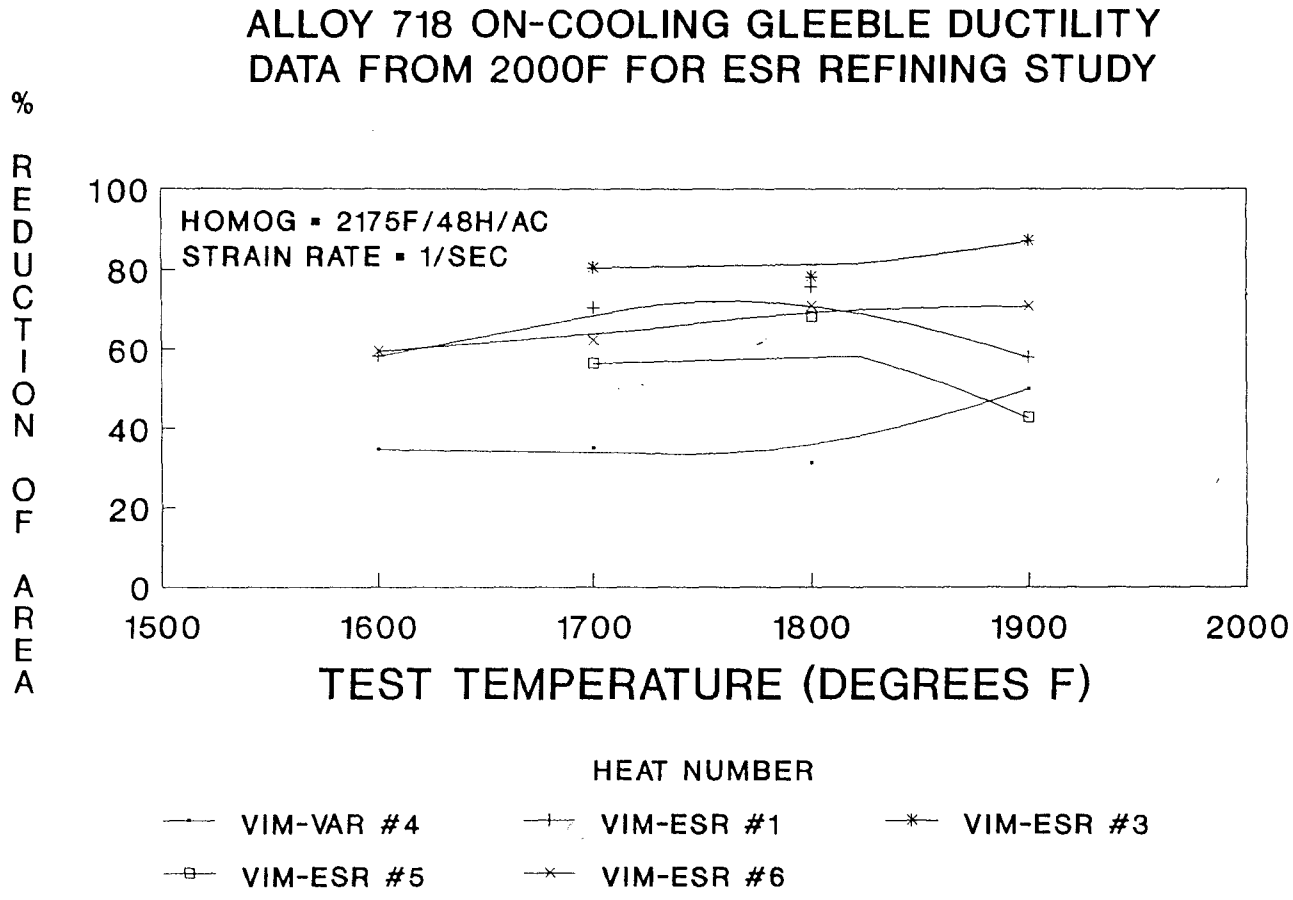

FIGURE 16 - **Composite of All Alloy 718 On-Cooling Gleeble Data from Pre-Heat Temperature of 2000F for ESR Refining Study**

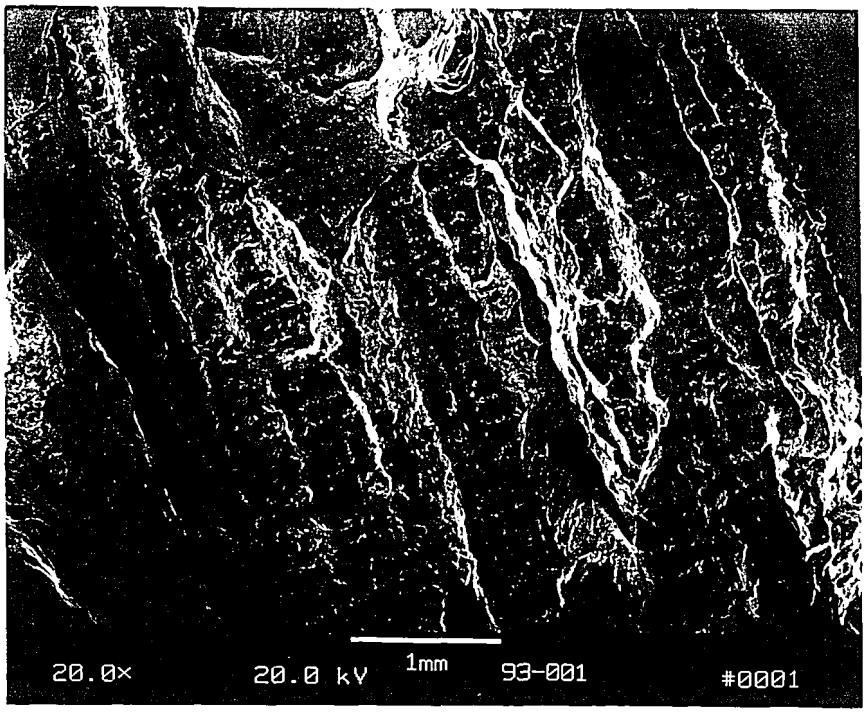

FIGURE 17 - Heat #4 On-Cooling Gleeble Specimen (2050→2000F) Fracture Face Showing 0% Reduction of Area. Note Appearance of Primary and Secondary Dendrites on Fracture Face and Smooth Fracture Surface Characteristic of Cleavage Fracture Mechanism.

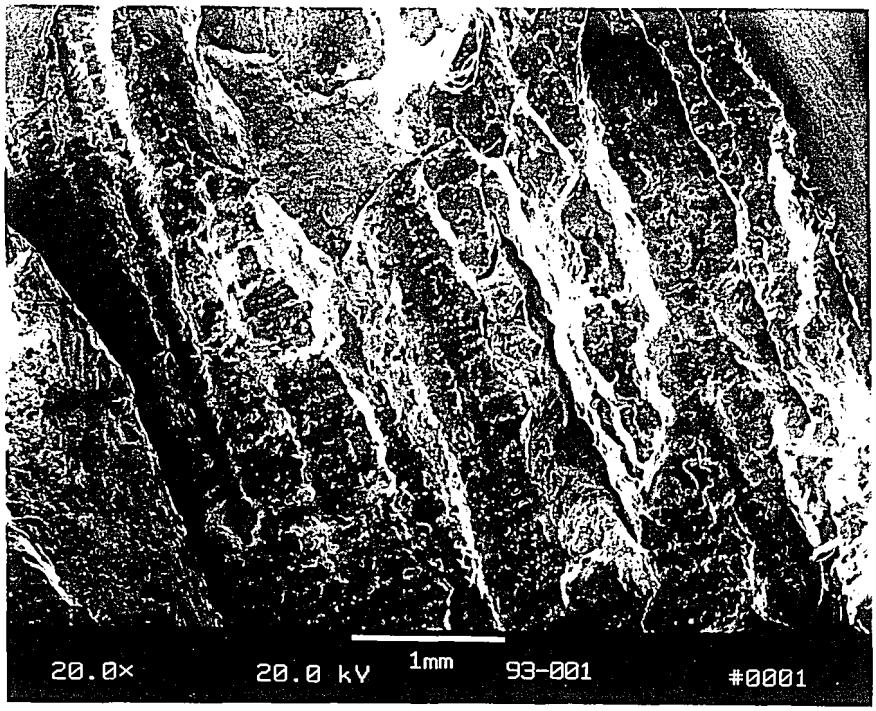

FIGURE 17 - Heat #4 On-Cooling Gleeble Specimen (2050→2000F) Fracture Face Showing 0% Reduction of Area. Note Appearance of Primary and Secondary Dendrites on Fracture Face and Smooth Fracture Surface Characteristic of Cleavage Fracture Mechanism.

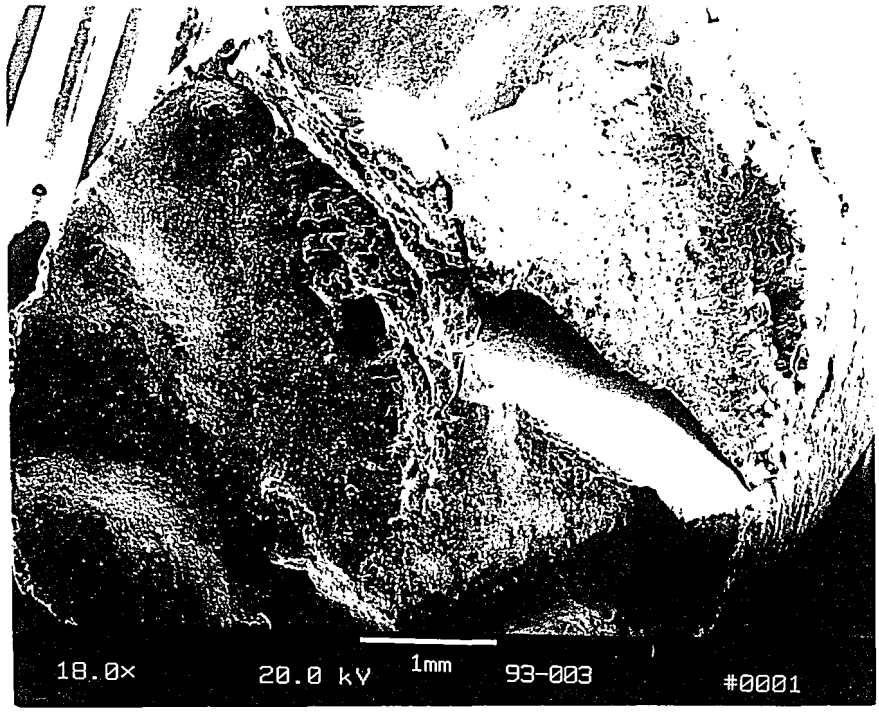

FIGURE 18A - Heat #5 On-Cooling Gleeble Specimen (2050→1700F) Fracture Face Showing 37.9% R.A. Note 45 Degree Shear Plane and Regions Showing Small Amount of Dimpling.

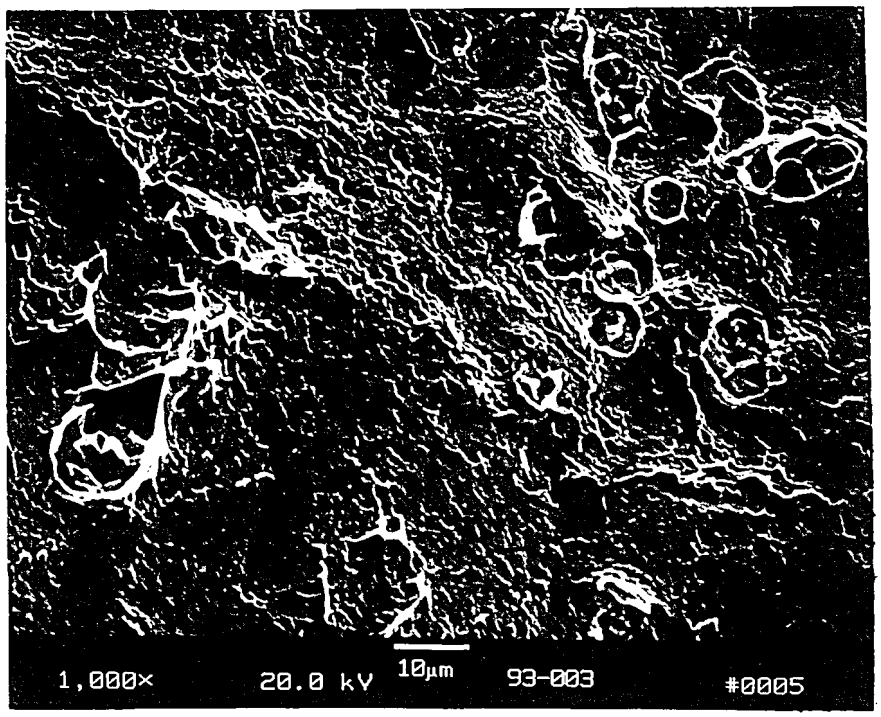

FIGURE 18B - Higher Magnification SEM Photomicrograph of Figure 18A Showing Small Amount of Dimpling on Fracture Surface

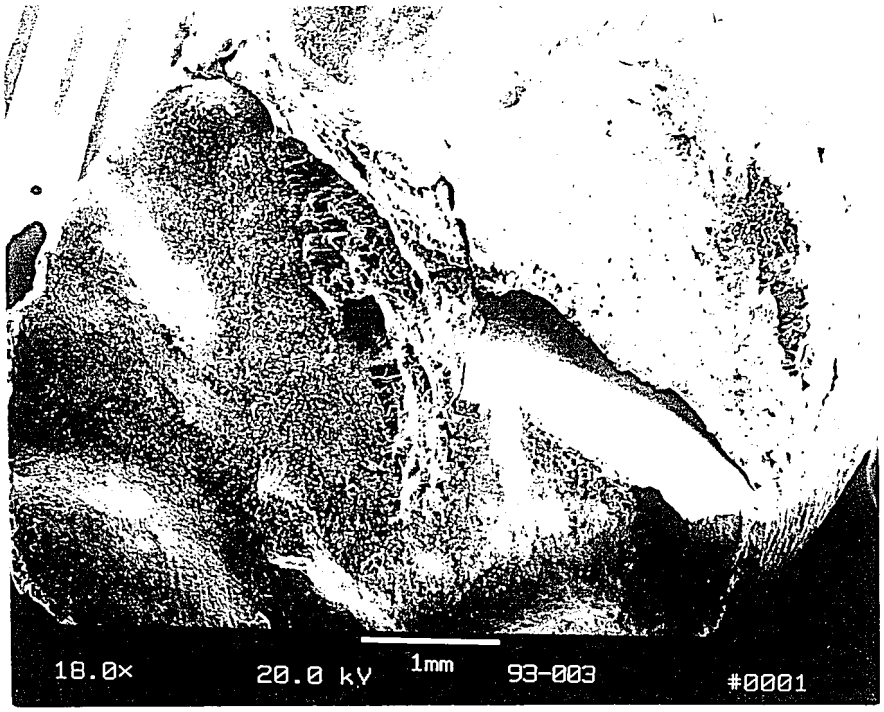

FIGURE 18A - Heat #5 On-Cooling Gleeble Specimen (2050→1700F) Fracture Face Showing 37.9% R.A. Note 45 Degree Shear Plane and Regions Showing Small Amount of Dimpling.

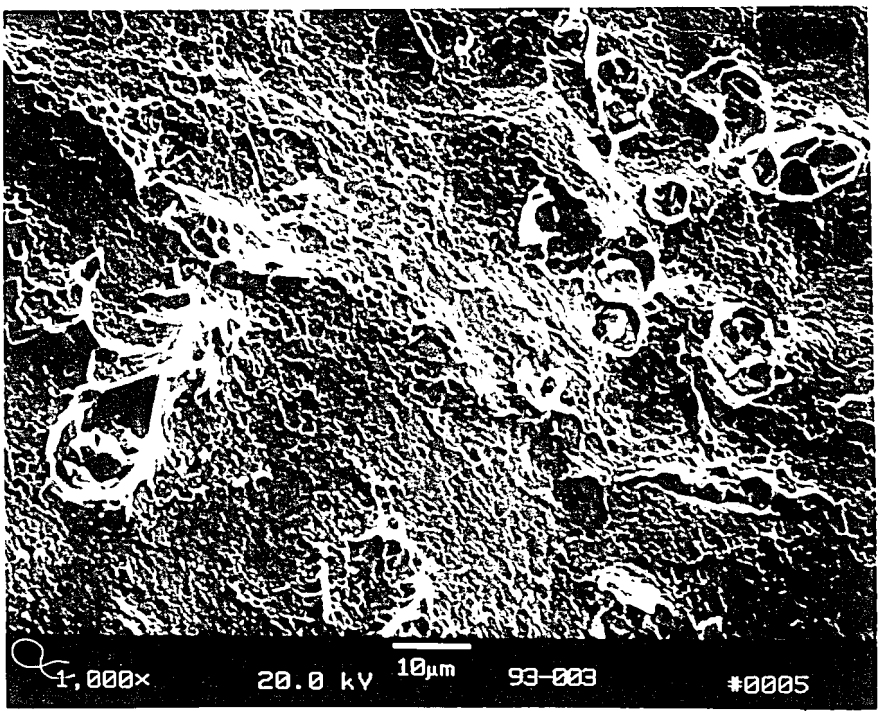

FIGURE 18B - Higher Magnification SEM Photomicrograph of Figure 18A Showing Small Amount of Dimpling on Fracture Surface

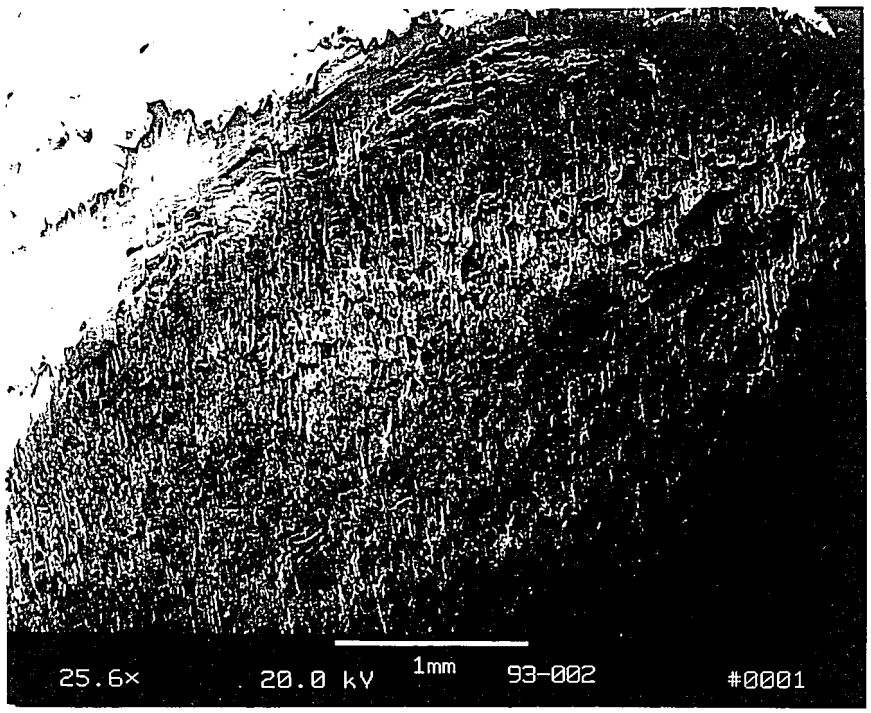

FIGURE 19A - Heat #5 On-Cooling Gleeble Specimen (2050→1700F) Fracture Face Showing 53% R.A. Note Most of Surface Exhibits Elongated Dimples.

FIGURE 19B - Higher Magnification SEM Photomicrograph of Figure 19A Showing Elongated Dimples on Fracture Face.

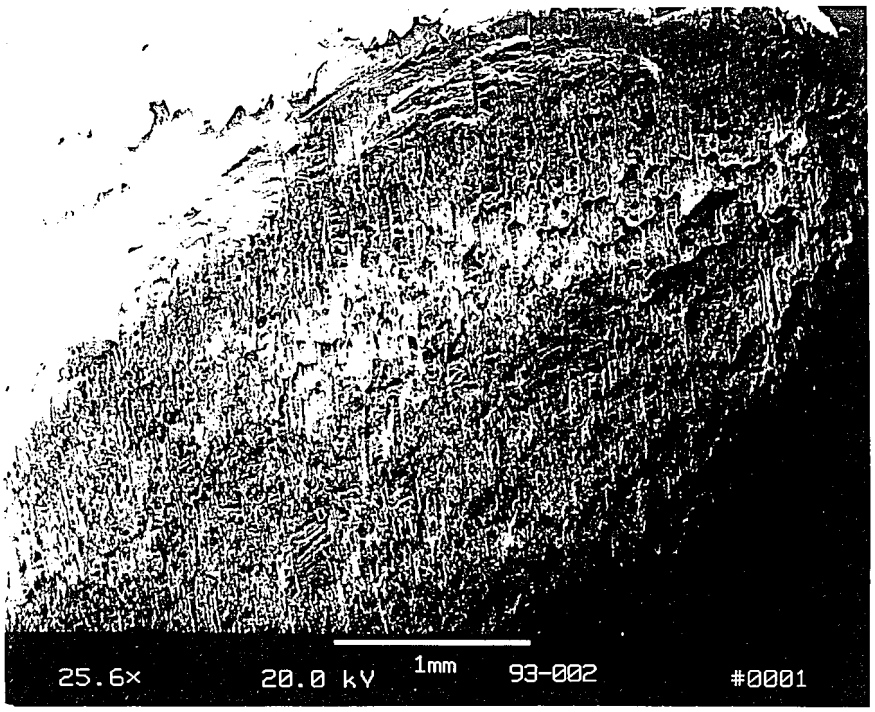

FIGURE 19A - Heat #5 On-Cooling Gleeble Specimen (2050→1700F) Fracture Face Showing 53% R.A. Note Most of Surface Exhibits Elongated Dimples.

FIGURE 19B - Higher Magnification SEM Photomicrograph of Figure 19A Showing Elongated Dimples on Fracture Face.

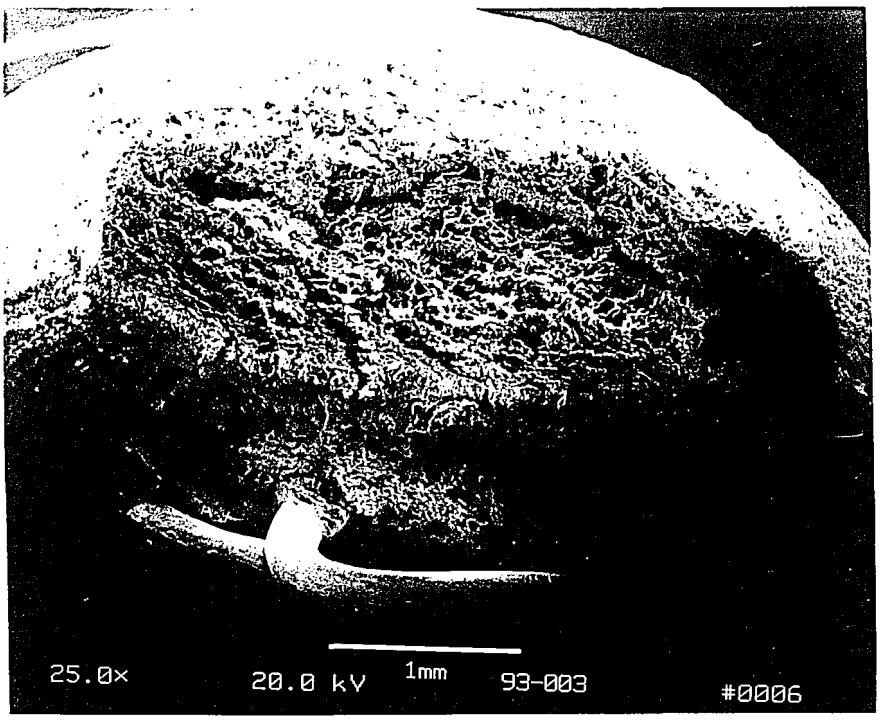

FIGURE 20A - Heat #3 On-Cooling Gleeble Specimen (2050→1800F) Fracture Face Showing 87.9% R.A. Note High Level of Dimpling Characteristic of High Ductility Microvoid Coalescence Fracture Mechanism.

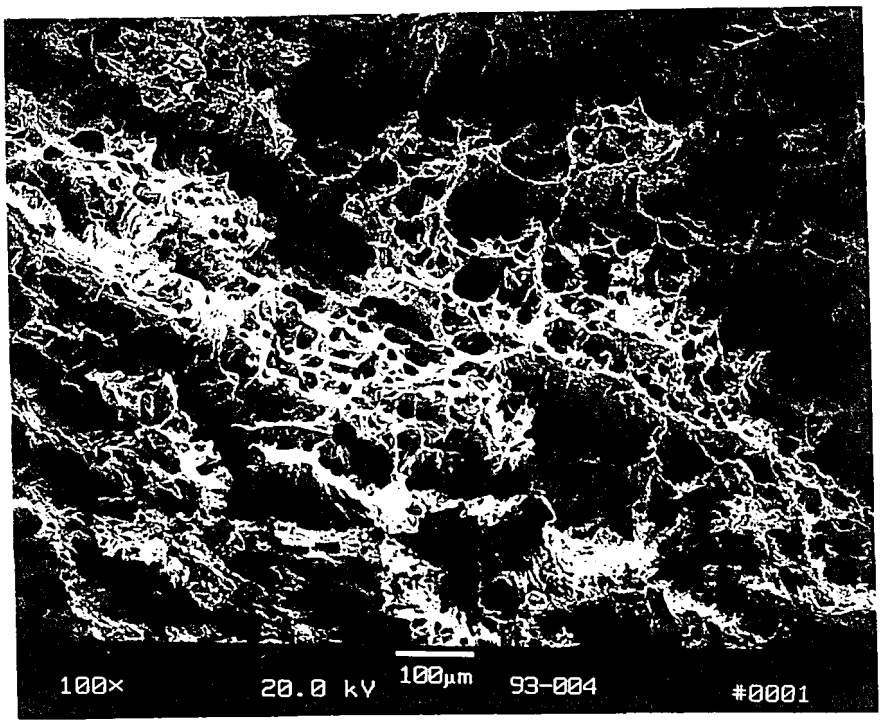

FIGURE 20B - Higher Magnification SEM Photomicrograph of Figure 20A Showing Extensive Dimples and Microvoids

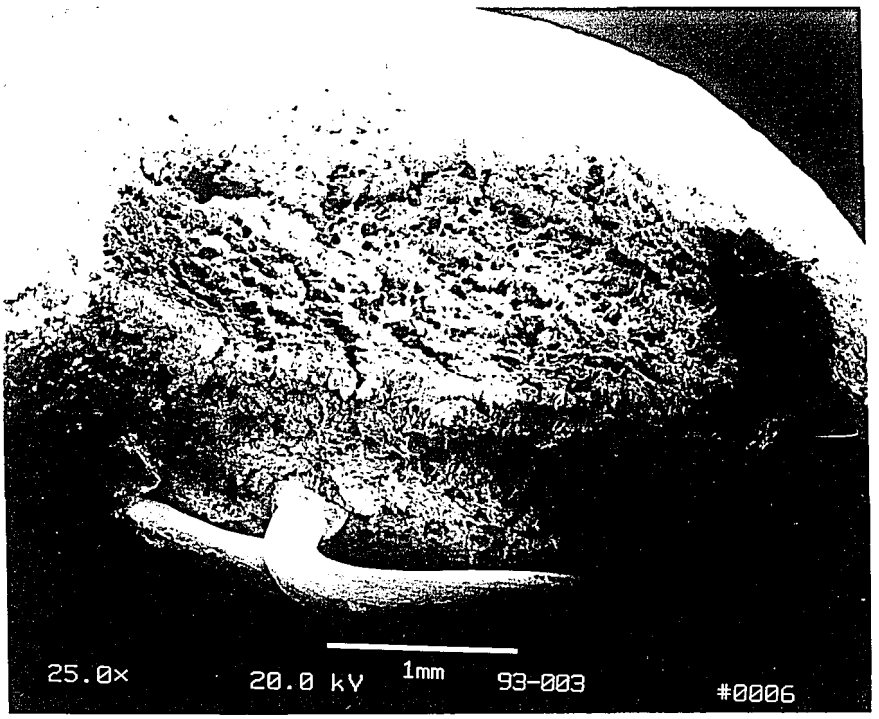

FIGURE 20A - Heat #3 On-Cooling Gleeble Specimen (2050→1800F) Fracture Face Showing 87.9% R.A. Note High Level of Dimpling Characteristic of High Ductility Microvoid Coalescence Fracture Mechanism.

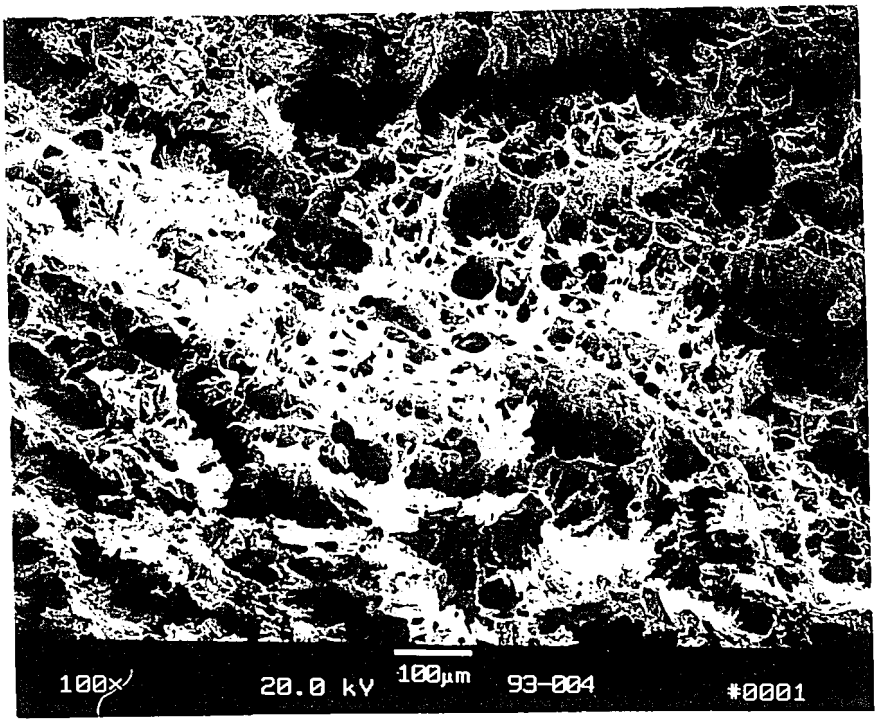

FIGURE 20B - Higher Magnification SEM Photomicrograph of Figure 20A Showing Extensive Dimples and Microvoids

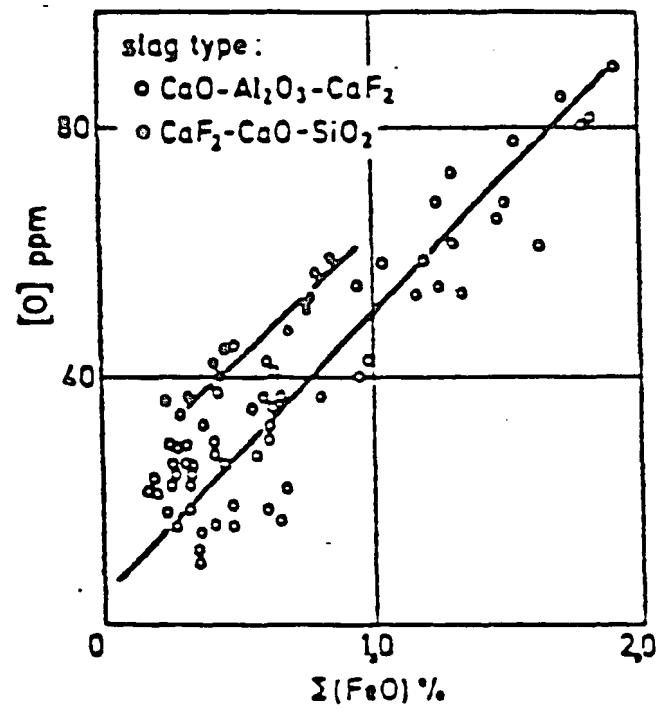

FIGURE 21 - Influence of Slag FeO Content on Oxygen Level in Metal Pool[9].

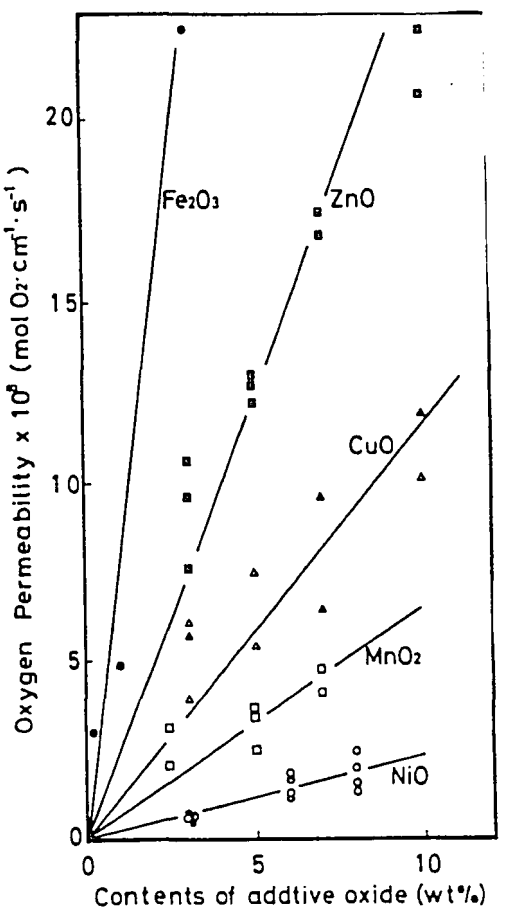

FIGURE 22 - Relationship Between Reference Oxygen Diffusing Rate, P, Through Molten $CaO-SiO_2$ - Al_2O_3 System Bearing One Oxide and Its Contents at 2640F[27].

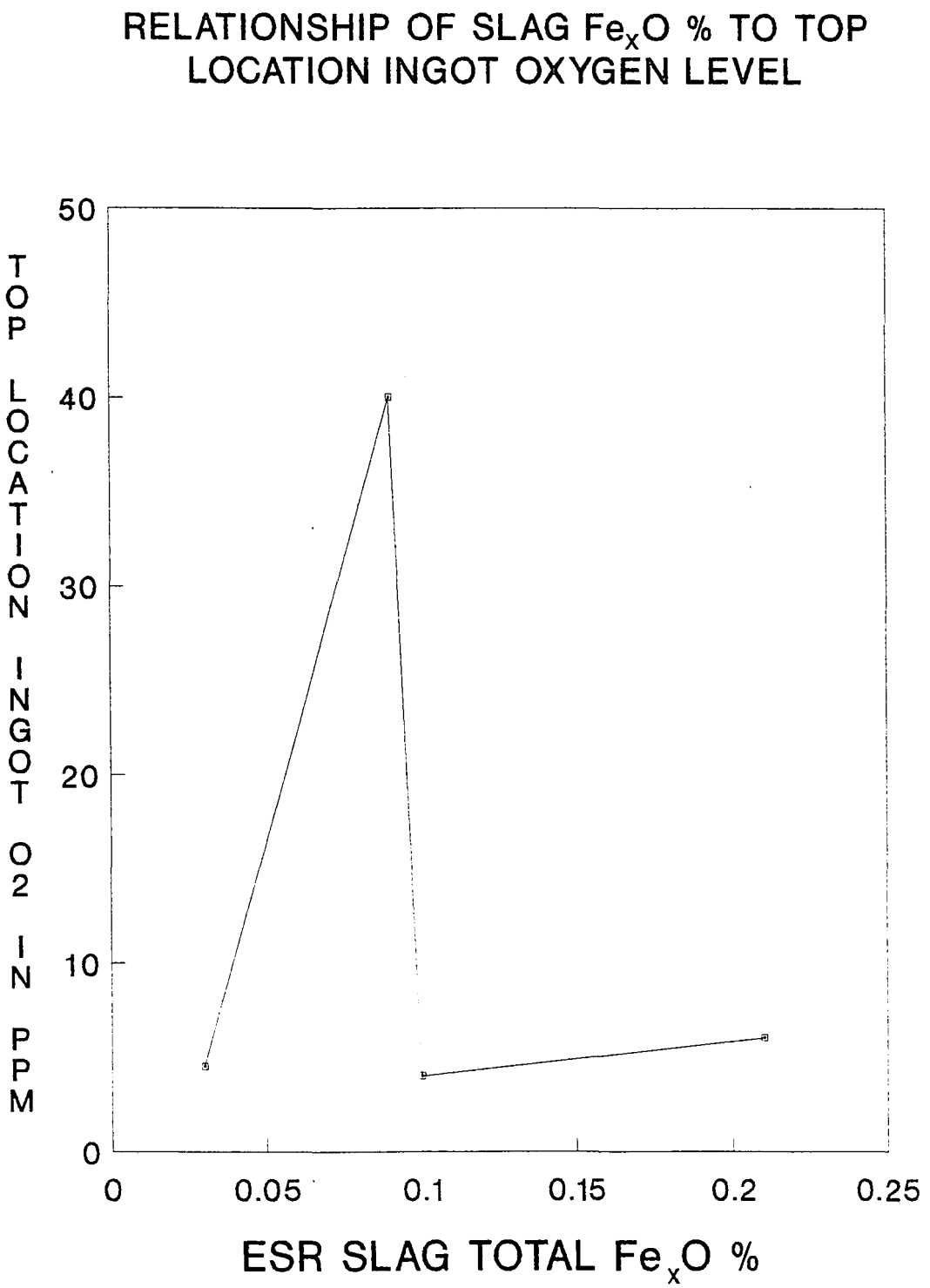

FIGURE 23 - Graph of Measured Slag FeO% to Ingot Oxygen Level at Top Location of VIM-ESR Ingots for ESR Refining Study.

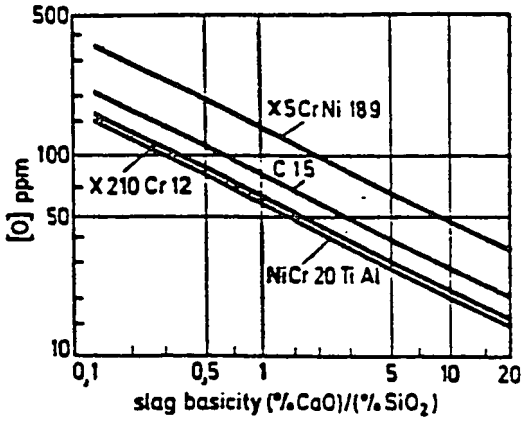

FIGURE 24 - Oxygen Levels for Various ESR Alloys Graphed as a Function of Slag Basicity[9].

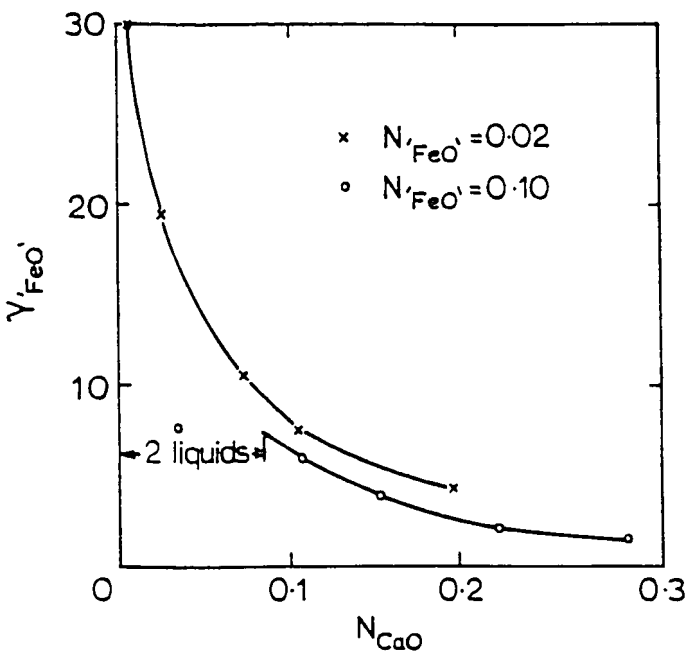

$\gamma Fe_{0.937}O$ v. N_{CaO} in CaF_2–CaO–FeO system at 1450°C

FIGURE 25 - FeO Activity Coefficient as a Function of CaO Level in CaF_2/CaO/FeO System at 2640F[26].

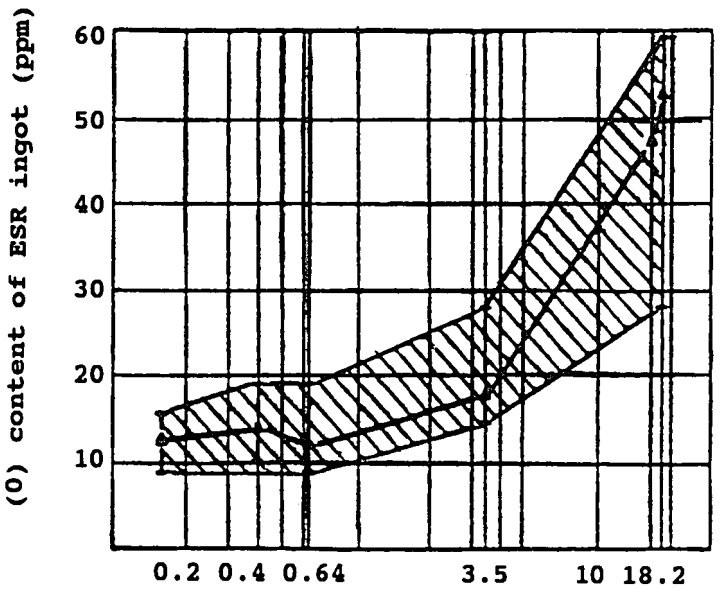

FIGURE 26 - Influence of Oxygen Content Above Slag Pool on Oxygen in ESR Ingot[9].

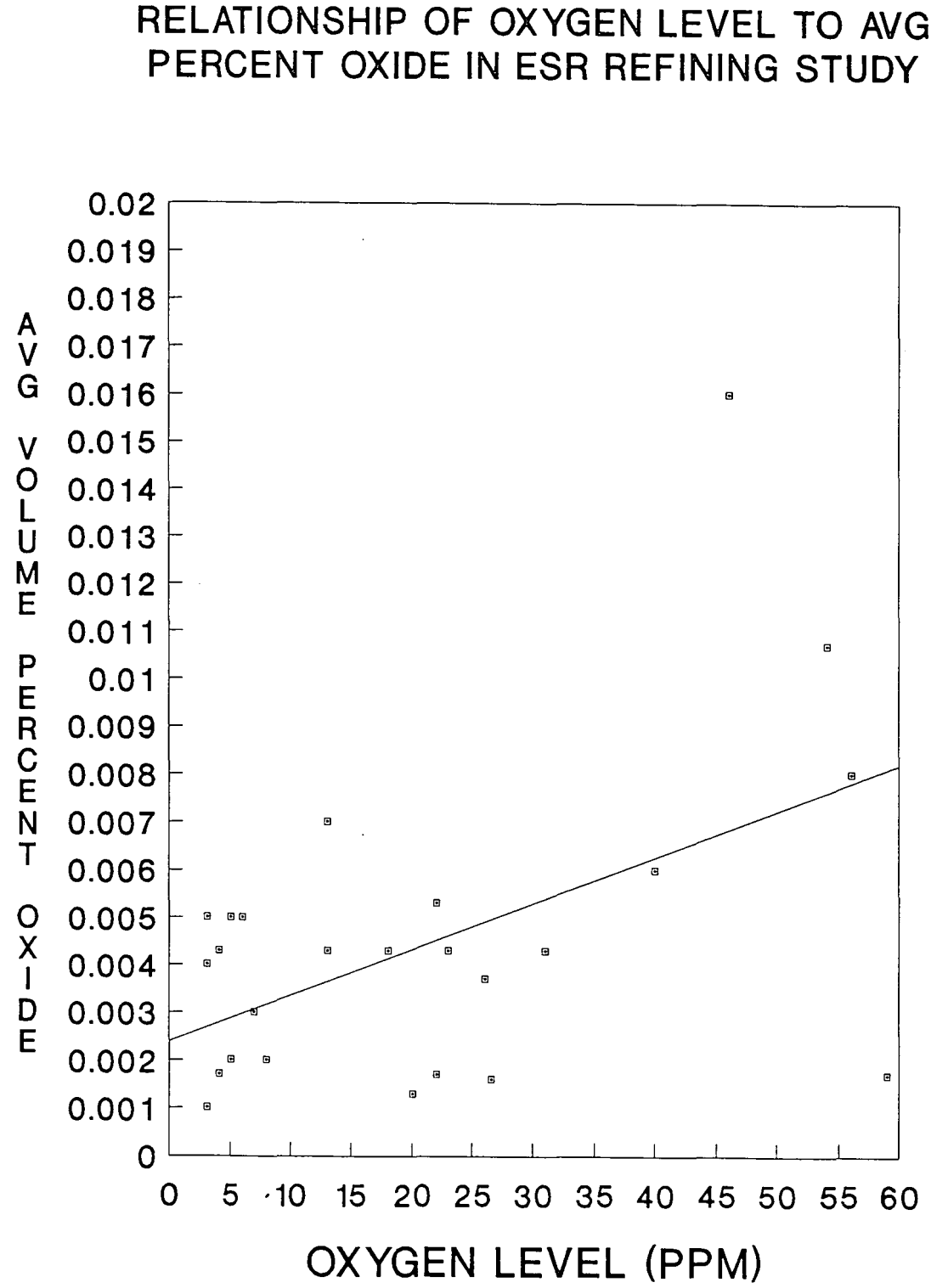

FIGURE 27 - Graph of Measured Oxygen Level to Average Volume Percent Oxide for all Ingot Locations in Alloy 718 ESR Refining Study.

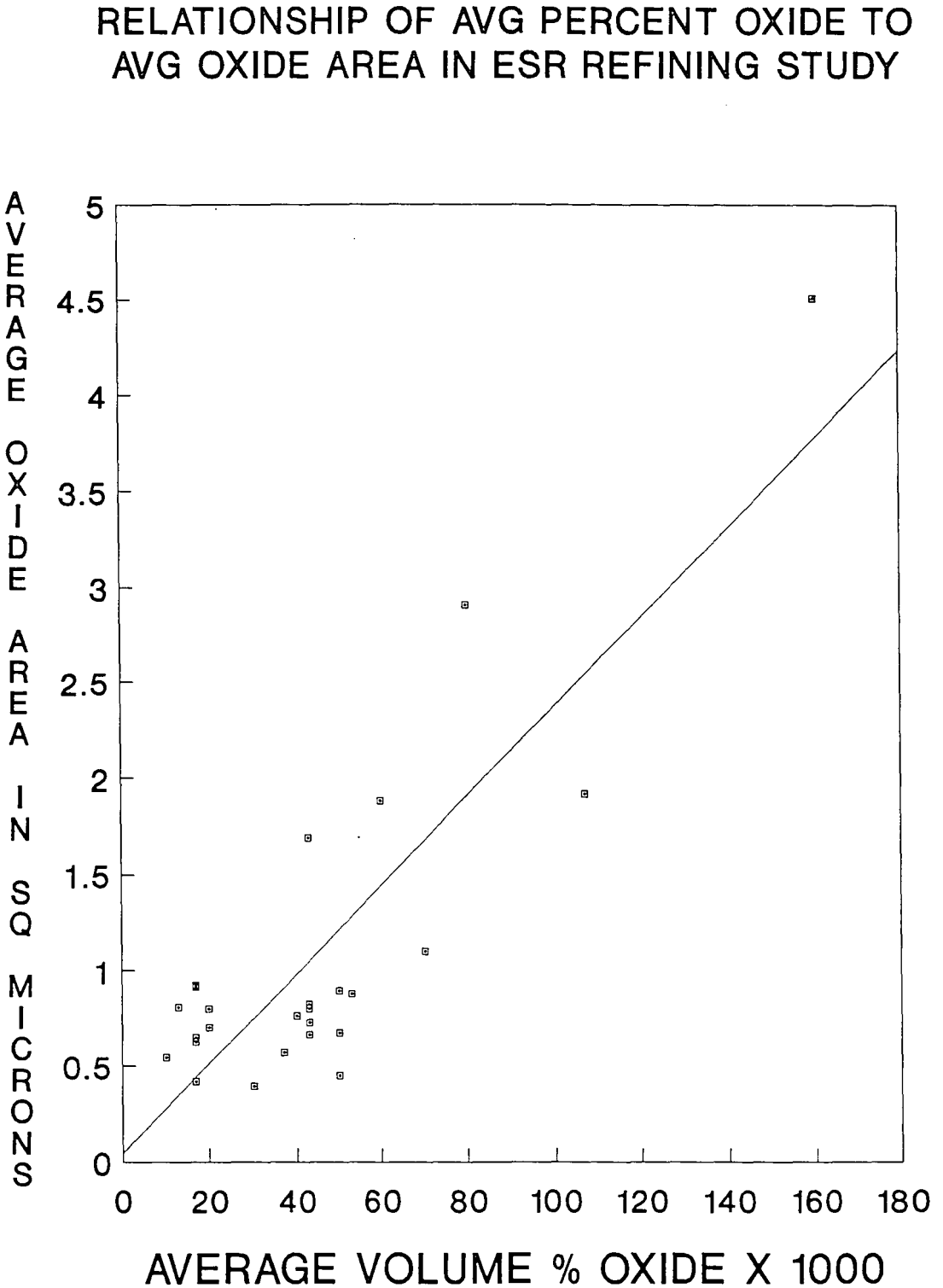

FIGURE 28 - Graph of Average Volume Percent Oxide vs. Average Oxide Area for all Ingot Locations in Alloy 718 ESR Refining Study.

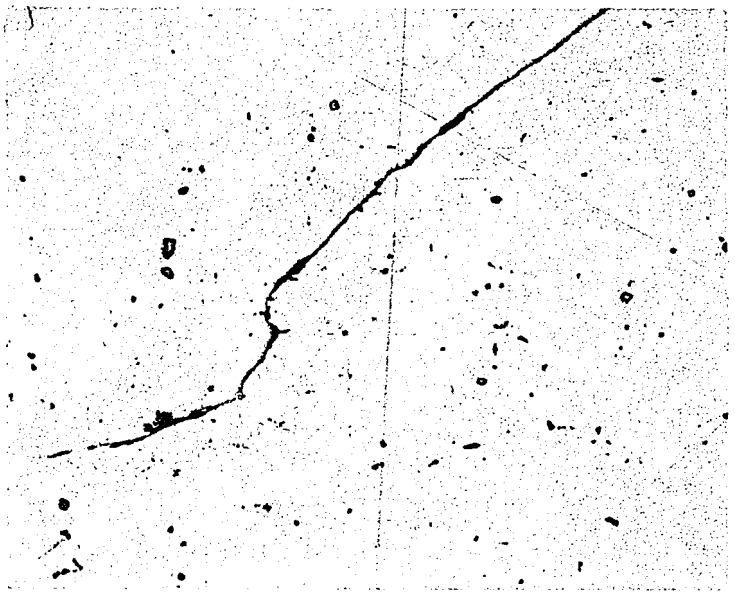

MAG: 100X ETCHANT: None
FIGURE 29A - Heat 3 Forged Bar Microstructure Showing Crack Root.

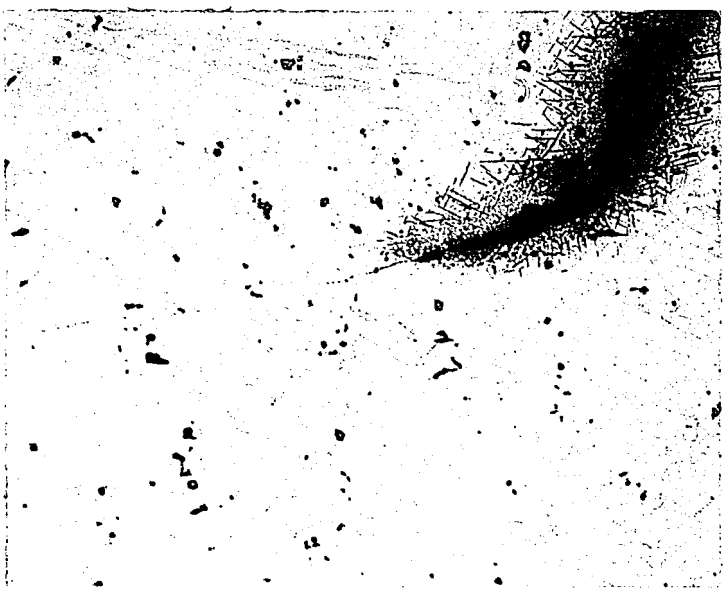

MAG: 100X ETCHANT: Glyceregia
FIGURE 29B - Same Crack Location as Shown in Figure 29A. Note that Crack Root is Following Grain Boundary Suggesting Grain Boundary Weakness or Embrittlement.

VITA

Dwight D. Wegman was born to Mr. and Mrs. Levi Wegman on March 23, 1960 in Reading, PA. He received his secondary education at Oley Valley High School, Oley, Pennsylvania and was elected a member of the National Honor Society. In the fall of 1978, he entered Drexel University and was awarded a Bachelor of Science Degree in Materials Engineering in June, 1983.

Since July 1983, he has been employed as a metallurgist by Carpenter Technology Corporation in Reading, Pennsylvania. During his tenure in the High Temperature Alloy Research Group, he co-invented a Heat and Corrosion Resistant Steel Alloy which was patented under U. S. Patent No. 4,929,419 and 5,019,332 and has authored two technical papers. Currently, his title is Senior Metallurgist, Process R & D.

The author currently resides in Reading with his wife Sharon and is very active in his church fellowship.

END

OF

TITLE